

Weak Diffusion Priors Can Still Achieve Strong Inverse-Problem Performance

Jing Jia ^{*1}, Wei Yuan ^{*2}, Sifan Liu³, Liyue Shen⁴, and Guanyang Wang²

¹Department of Computer Science, Rutgers University,
 jing.jia@rutgers.edu

²Department of Statistics, Rutgers University,
 {wy204, guanyang.wang}@rutgers.edu

³Department of Statistical Science, Duke University,
 sifan.liu@duke.edu

⁴Department of EECS, University of Michigan,
 liyues@umich.edu

February 2, 2026

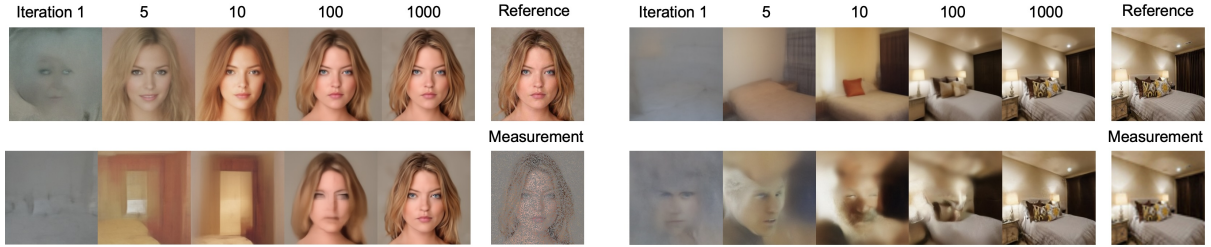


Figure 1: Image reconstruction using only a 3-step DDIM generator as the prior: matched prior (top) vs. mismatched prior (bottom). Diffusion models trained on bedroom images (resp. face images) can reconstruct face images (resp. bedroom images), shown in the bottom-left (resp. bottom-right) panels. From left to right, we display intermediate reconstructions over optimization iterations. The Reference column shows the clean image, and the Measurement column shows the noisy observation.

^{*}Equal contribution

Abstract

Can a diffusion model trained on bedrooms recover human faces? Diffusion models are widely used as priors for inverse problems, but standard approaches usually assume a high-fidelity model trained on data that closely match the unknown signal. In practice, one often must use a mismatched or low-fidelity diffusion prior. Surprisingly, these weak priors often perform nearly as well as full-strength, in-domain baselines. We study when and why inverse solvers are robust to weak diffusion priors. Through extensive experiments, we find that weak priors succeed when measurements are highly informative (e.g., many observed pixels), and we identify regimes where they fail. Our theory, based on Bayesian consistency, gives conditions under which high-dimensional measurements make the posterior concentrate near the true signal. These results provide a principled justification on when weak diffusion priors can be used reliably.

1 Introduction

Inverse problems aim to recover an unknown signal from noisy measurements. Recently, diffusion models have emerged as powerful *data-driven priors* for inverse problems, achieving state-of-the-art performance across a wide range of tasks in computer vision and related fields. The standard paradigm employs the same “full-strength” diffusion model as the prior: for example, a 1000-step DDPM [Ho et al. \(2020\)](#); [Song et al. \(2021b\)](#) trained on a face dataset to recover human faces. Building on this, existing solvers integrate the diffusion model directly into reconstruction by injecting measurement information throughout a reverse diffusion chain to enforce consistency with the observation ([Song et al., 2021b, 2022](#); [Chung et al., 2023](#); [Kawar et al., 2022](#); [Meng & Kabashima, 2022](#); [Zhou et al., 2024](#); [Song et al., 2024](#)). This strategy constitutes the mainstream approach for diffusion-based inverse problem solving.

However, the luxury of a perfectly matched, full-strength prior is often unavailable. Practical constraints often force us to use “weaker priors,” meaning diffusion models that are heavily truncated at inference or trained on a mismatched dataset. For example, [Wang et al. \(2024\)](#) and [Chihaoui et al. \(2024\)](#) propose optimizing the initial noise to solve inverse problems. To meet the memory constraints, they have to drastically truncate the diffusion process to just a few steps. Consequently, the prior itself is severely limited: it can only generate low-fidelity, blurry images (see [Iteration 1](#) in Figure 1). In parallel, in data-scarce domains such as medical image restoration, the absence of training data precludes the creation of domain-specific models. Therefore, researchers often compromise by relying on pre-trained models from completely mismatched distributions ([Knoll et al.,](#)

2019; Jalal et al., 2021; Glaszner & Zach, 2024; Aali et al., 2024; Hu et al., 2025; Barbano et al., 2025).

Surprisingly, these weak priors can still yield highly competitive reconstructions. For example, Wang et al. (2024) reports a 2–6 dB PSNR improvement over state-of-the-art baselines across a range of inverse problems, despite using only a 3-step DDIM prior Song et al. (2021a). Likewise, Jalal et al. (2021) shows that a diffusion prior trained exclusively on 2D brain MRI can still be used to reconstruct out-of-distribution scans such as knee and abdomen MRI.

These results raise a puzzle: standard intuition suggests that the quality of the reconstruction is bounded by the quality of the prior. Yet, in these regimes, weak priors perform nearly as well as, or even better than, stronger ones. At present, such successes are largely reported case by case in application-driven studies, and a systematic understanding of *when* and *why* weak priors suffice remains lacking.

Motivated by these observations, we ask: *can a low-fidelity bedroom diffusion model recover face images?* More broadly, we study when an inverse problem is robust to the choice of prior, in the sense that a low-quality or mismatched generative prior can still yield high-quality reconstructions, and when it cannot.

Our main contribution is a rigorous characterization of this phenomenon, supported by both empirical benchmarks and theoretical analysis. **Our central message** is that weak priors can still yield strong results in data-informative regimes, where observations are high-dimensional and the signal is identifiable from the measurements. In these settings, reconstruction is driven more by the observation than by the prior. Conceptually, this gives a novel insight that the prior may matter less than is often assumed when measurements are sufficiently informative. Practically, our findings justify using weak priors as a default when perfectly matched models are unavailable.

To support this, we provide:

1. **Empirical evidence:** We conduct extensive experiments across a variety of inverse problems, datasets, and diffusion backbones. We find that even severely truncated or mismatched priors can yield accurate reconstructions in data-informative regimes.
2. **Theory:** To explain this puzzle, we establish a framework rooted in Bayesian consistency that links measurement informativeness to reduced prior sensitivity. We formalize the information content of an observation through its effective observed dimensionality and the identifiability of the signal from the measurements. We prove that strong measurements can effectively “wash out” the influence of a weak prior.
3. **Failure modes:** Beyond the successful cases, we also study when weak priors fail. These include box inpainting and large-scale super-resolution. We support these

findings with both theory and experiments.

4. **Algorithmic refinements:** To realize the prior-robust behavior predicted by our theory, we refine initial-noise optimization with a new optimizer and an improved early-stopping rule, which stabilize reconstruction and avoid overfitting.

2 Weak diffusion generators as priors

2.1 Setup and our algorithm

Formulation: We study inverse problems of the form $y = \mathcal{A}(x) + \epsilon$, where $y \in \mathbb{R}^m$ denotes the observed data and $x \in \mathbb{R}^n$ is the unknown signal to be reconstructed. The map $\mathcal{A} : \mathbb{R}^n \rightarrow \mathbb{R}^m$ is called the *forward operator*, and $\epsilon \sim \mathcal{N}(0, \sigma^2 I_m)$ models additive Gaussian noise.

Diffusion prior: The mapping from x to y is typically many-to-one, so recovering x from y is ill-posed. To regularize the problem, we place a prior distribution π on x that captures the structure of plausible signals (e.g., natural images). In modern generative modeling, such a prior is often specified through a pretrained generator G that maps Gaussian noise to a sample in data space. In this paper, we focus on diffusion-based generators, where G is realized by a finite number of reverse diffusion steps (e.g., a k -step DDIM sampler).

Weak prior: Most prior work uses the original *full diffusion model* as a prior, trained on data whose *distribution closely matches the target signals*. When either of these two conditions is not met, we call the resulting prior *weak*. More precisely, weak diffusion priors may arise from two sources:

- *Low-quality generator:* G is obtained by running only a few reverse steps (e.g., a 1–4 step DDIM sampler), which typically yields low-fidelity samples.
- *Dataset mismatch:* The generator is trained on a distribution different from the target data.

Imagine a task of recovering human faces. A 3-step DDIM generator trained on a face dataset is weak because it produces low-fidelity samples (see the top-left image in Figure 1). A 3-step DDIM generator trained on a bedroom dataset is also weak because it is both low-quality and mismatched to the target distribution (see the bottom-left image in Figure 1).

Diffusion inverse problem solvers: Given a diffusion prior π and measurement model $y = \mathcal{A}(x) + \epsilon$, the goal is to characterize the posterior $\pi(x | y)$. In practice, one

can approximately sample from $\pi(x | y)$ or compute the maximum a posteriori (MAP) estimate $\arg \max_x \pi(x | y)$.

Most existing solvers use the *full diffusion model* as the prior and follow a similar recipe: at each step, they adjust the backward update to incorporate information from the observation y and the measurement model. This adjustment has been implemented in many ways, such as guidance, variable splitting, and sequential Monte Carlo; see [Zheng et al. \(2025\)](#) for a summary. Among them, diffusion posterior sampling (DPS) [Chung et al. \(2023\)](#) is one of the most popular solvers, so we take it as our baseline.

Initial noise optimization: Another line of work treats the generative model G as a black-box generator and solves inverse problems by optimizing the latent input. Given an observation y , it computes

$$\arg \min_z L(\mathcal{A}(G(z)), y) + \lambda \mathcal{R}(G(z)), \quad (1)$$

where L measures the mismatch between the simulated measurement $\mathcal{A}(G(z))$ and y , and \mathcal{R} is a regularizer.

This latent-optimization view is conceptually simple and dates back to work on GANs and VAEs [Bora et al. \(2017\)](#). However, when G is a full diffusion model, optimizing (1) requires backpropagating through tens to hundreds of sampling steps, which is often too costly in memory and compute. As a result, prior work has to use a very weak generator G (e.g., a 1–4 step DDIM sampler) ([Wang et al., 2024](#); [Chihaoui et al., 2024](#)). Surprisingly, such inverse problem solvers based on weak generators can outperform full diffusion step-modification methods, which motivates our study.

Beyond inverse-problem tasks, initial-noise techniques have recently attracted interest across a range of applications for their potential to support inference-time scaling; see [Ben-Hamu et al. \(2024\)](#); [Jia et al. \(2025\)](#); [Ma et al. \(2025\)](#); [Zhou et al. \(2025\)](#); [Wan et al. \(2025\)](#); [Tang et al. \(2025\)](#).

AdamSphere and HoldoutTopK early stopping: Two factors, concentration and overfitting, affect the solution quality of (1). First, diffusion models are trained with $z \sim \mathbb{N}(0, I_d)$, whose mass in high dimension concentrates near the sphere $\|z\| \approx \sqrt{d}$ [Vershynin \(2018\)](#). Unconstrained optimization can push z off this typical shell and degrade reconstruction quality. We therefore propose **ADAMSPHERE**, a modified ADAM optimizer that keeps z on the sphere throughout. Second, it has been observed ([Wang et al., 2024](#)) that latent optimization can overfit measurement noise. We propose **HOLDOUTTOPK** early stopping. We hold out a subset of measurements (not used in optimization) and track its loss at each iteration. We then return the latest iterate among the best K holdout losses. Our idea is inspired by statistical machine learning, where a validation set is used

to approximate test performance and guide model selection. However, unlike the usual practice in machine learning of selecting the single lowest-validation-error candidate, we keep the top- K and return the latest iterate among them. We find that $K > 1$ reduces sensitivity to noisy fluctuations while still selecting a near-best checkpoint that generalizes to the holdout set.

Since `ADAMSPHERE` already constrains the iterates to lie on the sphere, we optimize only the mean-squared error (MSE):

$$\arg \min_z \|\mathcal{A}(G(z)) - y\|^2. \quad (2)$$

Section 3.2 shows that, under suitable assumptions, minimizing (2) is equivalent to steering the posterior toward the correct mode. The details of `ADAMSPHERE` and `HOLD-OUTTOPK` are given in Appendix B. Section 4.2 presents ablation studies demonstrating their effectiveness.

2.2 Main observations:

Our main observation is that weak diffusion generators can still deliver strong performance on many practical inverse problems. Figure 1 shows representative examples. The left panel illustrates an inpainting task on a human face using two different weak priors, where the observed image (measurement) is obtained by masking a large fraction of pixels and adding Gaussian noise to the remaining pixels. The reference column shows the clean image, but it is never used by the reconstruction algorithm. Both rows use a 3-step DDIM prior: the prior in the top row (in the left panel) is trained on human face images, while the prior in the bottom row is trained on bedroom images. We reconstruct the noisy image using the initial-noise optimization procedure in Section 2.1, and show intermediate reconstructions at optimization iterations 1, 5, 10, 100, and 1000. In particular, **Iteration 1** corresponds to the unconditional 3-step DDIM sample, before any optimization is performed.

The priors in both rows are “weak.” In the top row, the prior is in-distribution but low quality: the unconditional sample captures the rough outline of a face, but most colors and finer details are missing. The bottom row uses an even weaker, out-of-distribution prior: the unconditional sample is a low-quality sketch of a bedroom image. Nevertheless, as optimization proceeds, both priors quickly fit the measurement and converge to reconstructions that are both visually similar and accurate. The trajectory under the bedroom-trained prior is especially striking: early iterates look like a bedroom scene with straight edges and box-like shapes; but as optimization goes on, these features fade and the image gradually turns into a human face, with smoother contours and more

detail. This firmly answers the question at the beginning of our paper: even a low-fidelity diffusion model trained on bedrooms can recover face images.

The right panel of Figure 1 shows a super-resolution experiment with similar conclusions. These examples are only a small sample of our study. In Section 4.1, we present larger-scale evaluations across multiple tasks, comparing weak priors against strong-prior baselines. Overall, the results suggest that weak diffusion priors can match strong-prior baselines in data-informative regimes.

3 When data dominates the prior

Now we theoretically study when the posterior is mainly driven by the observation, so that even substantial changes in the prior have little impact on the reconstruction. We first review the classical i.i.d. case in Section 3.1, where posterior consistency shows how increasing sample size can overwhelm prior differences. Section 3.2 studies the single-observation, high-dimensional inverse-problem regime using a Gaussian-mixture surrogate for the prior. Under a δ_0 -identifiability assumption, we show that high-dimensional measurements force the posterior to concentrate at an exponential rate around the true signal. Beyond the success regime, our analysis also clarifies the failure modes.

3.1 Posterior consistency under i.i.d. data

We first recall a standard phenomenon in Bayesian inference: under an i.i.d. model, sufficiently informative data can dominate the prior. Consider the linear inverse problem $y = Ax + \epsilon$, where ϵ is the standard Gaussian noise. In a synthetic experiment, we fix a ground-truth signal x^* , draw a linear operator A , and generate i.i.d. observations $y_{1:N}$. We then place two well-separated Gaussian-mixture priors π_A and π_B on x (Figure 2 left panel). Despite their large difference, as N increases both posteriors $\pi_A(\cdot | y_{1:N})$ and $\pi_B(\cdot | y_{1:N})$ concentrate around x^* , as shown in the right two panels of Figures 2.

This is an instance of *posterior consistency*. At a high level, the posterior is determined by both the prior and the data. As the data become increasingly informative (here, as the sample size grows), the likelihood term ultimately overwhelms the prior. Thus, even when the priors are very different, the resulting posteriors can still both concentrate on the same ground-truth signal. A classical result due to [Schwartz \(1965\)](#) makes this precise. For readability, assumptions and the exact convergence notion are deferred to the Appendix A.1.

Theorem 3.1 (Posterior consistency, informal). *Let $\{P_x\}_{x \in \mathcal{X}}$ be a statistical model and let Y_1, Y_2, \dots be i.i.d. from P_{x^*} . Under standard regularity and identifiability assumptions,*

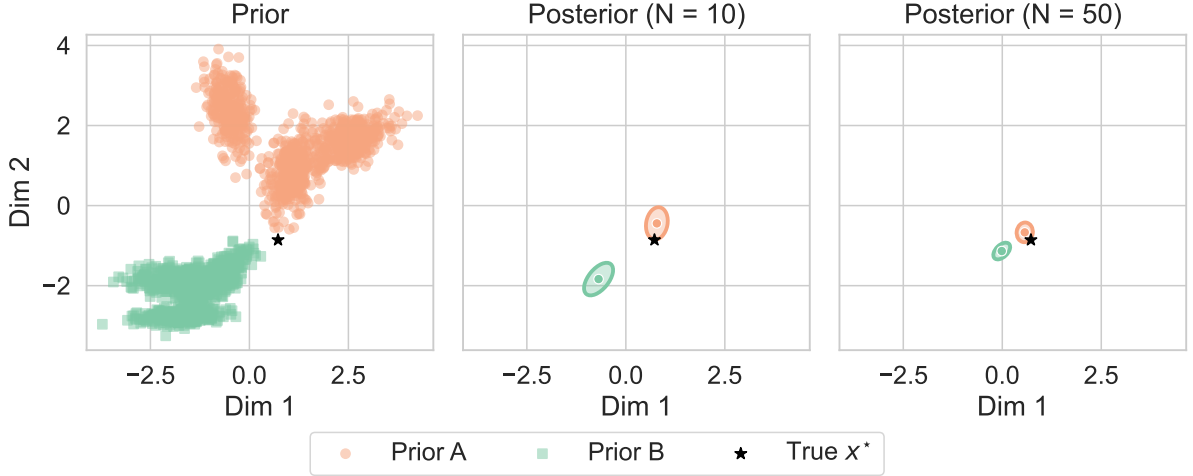


Figure 2: Posterior concentrates around x^* as N grows.

and assuming the prior π puts positive mass in every neighborhood of x^* , the posterior $\pi(\cdot | y_{1:N})$ concentrates at x^* as $N \rightarrow \infty$.

Theorem 3.1 shows that, under the i.i.d. model, the effect of the prior becomes negligible as the sample size grows. While insightful, the i.i.d. setting differs from image inverse problems, where measurements (pixels) are strongly dependent and we typically have only a single observation y^* . The next section develops theory to study the posterior behavior in high-dimensional, single-observation regime.

3.2 High dimensional inverse problem under generative prior

We continue to study the linear inverse problem $y = Ax + \epsilon$, where $x \in \mathbb{R}^n$, $A \in \mathbb{R}^{m \times n}$, and $\epsilon \sim \mathcal{N}(0, \sigma^2 I_m)$. Throughout, we focus on the practically relevant regime where only a *single* observation y^* is available (e.g., one corrupted image), while the measurement dimension m is large (e.g., $512 \times 512 \times 3$). Our goal is to understand when the posterior is *robust* to the choice of generative prior, so that substantially different priors can still yield similar reconstructions.

Throughout this section, we use $\varphi(\cdot, \mu, \Sigma)$ to denote the density of $\mathcal{N}(\mu, \Sigma)$.

A tractable model for generative priors. Modern generative priors such as k -step DDIM do not admit a tractable density. However, in practice their samples tend to lie near the data manifold, in the sense that generated images are often close to plausible clean-image prototypes. Motivated by this, a common surrogate is to model the prior as a Gaussian mixture. Finite Gaussian mixture models can approximate a broad class of distributions arbitrarily well (McLachlan & Peel, 2000). They are therefore widely adopted in studies of diffusion models, see Shah et al. (2023); Wu et al. (2024); Gatmiry et al. (2024); Liang et al. (2025). In particular, we assume the prior is an isotropic Gaussian

mixture

$$\pi(x) = \sum_{j=1}^M w_j \varphi(x; \mu_j, \tau^2 I_n). \quad (3)$$

Here, $\{\mu_j\}_{j=1}^M$ are the component means, which can be interpreted as the universe of clean data. We interpret *different generative priors* as different collections of weights $\{w_j\}_{j=1}^M$. Assuming all components share a common variance τ^2 keeps the core mathematics intact while keeping the argument clean. In the Appendix, we extend the model to allow component-specific (heterogeneous) variances.

Posterior collapse to the best-scoring mode. Given an observed y^* , it is known that the posterior remains a Gaussian mixture. The posterior weight of component j is proportional to $\tilde{w}_j := w_j \cdot \varphi(y^*; A\mu_j, \Sigma)$, where $\Sigma := \sigma^2 I_m + \tau^2 A A^\top$. See Appendix A.2 for a proof.

For each component j , define the *score* as the squared measurement residual

$$s_j(y^*) := \frac{1}{2} \left\| \Sigma^{-1/2} (y^* - A\mu_j) \right\|_2^2. \quad (4)$$

Let $s_{(1)}(y^*)$ and $s_{(2)}(y^*)$ be the lowest and second-lowest scores. We define the *per-dimension score gap* as

$$\delta(y^*) := \frac{1}{m} \left(s_{(2)}(y^*) - s_{(1)}(y^*) \right). \quad (5)$$

The following theorem states that, as m grows, the posterior concentrates on the component with the smallest score.

Theorem 3.2. *With the notation above, assume:*

1. (Bounded weight ratio) *There exists $C > 1$ such that $1/C \leq w_i/w_j \leq C$ for all (i, j) .*
2. (δ_0 -identifiable) *There is a unique minimizer $j^* = \arg \min_j s_j(y^*)$, and the score gap $\delta(y^*) \geq \delta_0$ for a constant $\delta_0 > 0$.*

Let J be a categorical random variable on $\{1, 2, \dots, M\}$ with $\mathbb{P}(J = j) := \tilde{w}_j / (\sum_{i=1}^M \tilde{w}_i)$, i.e., J indexes the component selected in the Gaussian mixture posterior. Then

- *The probability of not selecting the lowest score component satisfies*

$$\mathbb{P}(J \neq j^*) \leq CM \exp(-\delta_0 m).$$

- *The posterior concentrates onto the j^* -th Gaussian component at an exponential rate in the measurement dimension m :*

$$\|\pi(\cdot | y^*) - \mathbb{N}(m_{j^*}(y^*), \Sigma_{post})\|_{\text{TV}} \leq CM \exp(-\delta_0 m),$$

where $m_{j^*}(y^*) = \mu_{j^*} + \tau^2 A^\top \Sigma^{-1} (y^* - A\mu_{j^*})$, $\Sigma_{post} = \tau^2 I_n - \tau^4 A^\top \Sigma^{-1} A$, TV stands for total-variation distance.

Interpretation. Theorem 3.2 shows that if the best-matching component is δ_0 -identifiable, then the posterior concentrates overwhelmingly on this component, with the remaining mass decaying exponentially in dimension m . A simple intuition for Assumption 2 is: in image inverse problems like random inpainting, once many pixels are observed, incorrect candidate images often disagree with the observation in many places (edges, textures, colors), so the best-matching candidate becomes clearly separated.

Notably, Theorem 3.2 is largely insensitive to the particular choice of generative prior: as long as the mixture weights are bounded within constant factors, the prior affects the bound only through constants. Therefore, in the data-informative regime (i.e., when Assumption 2 holds) and with high-dimensional observations (large m), very different priors can still yield similar reconstructions, with the posterior concentrating on the same mode.

Score and MSE. We remark that the score in (4) coincides (up to a constant factor) with the MSE in many practical inverse problems. This justifies our optimization procedure (2) used in Section 2.1: minimizing the MSE is often equivalent to minimizing the score.

For inpainting problems, the measurement operator $A = P_\Omega$ is a coordinate projection (i.e., it selects a set Ω of the observed pixels), so $AA^\top = I_m$ and the Σ simplifies to $(\sigma^2 + \tau^2)I_m$. Therefore,

$$s_j(y^*) = \frac{1}{2(\sigma^2 + \tau^2)} \sum_{i \in \Omega} (y^{*,i} - \mu_{j,i})^2,$$

which is exactly the MSE restricted to observed pixels.

For super-resolution, the measurement operator A produces a low-resolution image $y \in \mathbb{R}^m$ from a high-resolution signal $x \in \mathbb{R}^n$ by averaging over non-overlapping downsampling blocks: each row of A has k nonzero entries with weights $1/k$, the row supports are disjoint, and $m \approx n/k$. Therefore, $AA^\top = k^{-1}I_m$, and the score simplifies to $s_j(y^*) = (2k(\sigma^2 + \tau^2))^{-1} \|y^* - A\mu_j\|_2^2$, which is again proportional to the MSE.

Justifying the identifiable assumption. We justify the δ_0 -identifiable assumption using both theory and empirical results. We evaluate three datasets: CelebA, Church, and Bedroom. For each image (with pixel values normalized to $(-1, 1)$), we generate an inpainting observation by masking 70% of pixels and adding Gaussian noise to the remaining pixels. For each resulting observation, we apply the same forward mask to every image in the dataset and compute the MSE on the observed pixels (which is proportional to the score). We then compute the per-dimension MSE gap for each image and report

aggregated gap statistics in Table 1.

These results indicate a clear separation: the mean per-dimension gap is about 0.22–0.28. Interpreting this as a per-pixel squared difference, it corresponds to an average absolute difference of at least ($\sqrt{0.22} \approx 0.47$) on the observed entries; since each pixel lies in $[-1, 1]$ (range 2), this is a substantial mismatch. Moreover, the gap stays bounded away from zero even in the worst case: the minimum per-dimension MSE gap over all images is at least 0.09 (average absolute difference of at least 0.3). Thus, these suggest that the best-matching candidate is typically well separated from the runner-up. In Appendix A.4, we provide a theoretical justification for Assumption 2 using concentration inequalities.

Failure modes. Our analysis also provides insights into when weak diffusion generators *fail* as priors.

Firstly, in large *box inpainting* (where A masks a contiguous block), many images can match the observed pixels closely while differing a lot inside the missing box. In this setting, the per-dimension score gap in Assumption 2 can be made arbitrarily small. Thus the data alone does not force the posterior to concentrate on a single mode. The reconstruction then becomes unavoidably prior-dominated and needs strong semantic generation to fill in the missing region.

Secondly, the upper bound in Theorem 3.2 is $M \exp(-\delta_0 m)$, scaling linearly in M and decaying exponentially in the number of observed entries m . When m is large, the exponential decay typically dominates; for 70% inpainting on a 256×256 image, $m \approx 256 \times 256 \times 30\% \times 3 \approx 60,000$. When m is small, the M factor can dominate; for $\times 16$ super-resolution, m can be as low as $16 \times 16 \times 3 = 768$. In this low-information regime, reconstruction is much more sensitive to the prior.

We empirically validate these failure modes in Section 4.3.

4 Experiments

We evaluate our method on four tasks: inpainting, Gaussian deblurring, super-resolution, and nonlinear deblurring with additive Gaussian noise. For each subsection, we report the subset of tasks most relevant to the setting under study, while full results across all tasks are provided in Appendix C. We evaluate each method using standard metrics, including PSNR, SSIM, and LPIPS [Zhang et al. \(2018\)](#).

Unless otherwise stated, all experiments are conducted using publicly available pre-

Table 1: Random inpainting score gap

Dataset	Mean (Std)	Min
CelebA	0.22 (0.06)	0.11
Church	0.28 (0.06)	0.15
Bedroom	0.27 (0.07)	0.09

trained diffusion checkpoints for the Bedroom (LSUN-Bedroom [Yu et al. \(2015\)](#)), Church (LSUN-Church [Yu et al. \(2015\)](#)), and Human face (CelebA [Liu et al. \(2015\)](#)) datasets. For each setting, we randomly select 100 test images for evaluation. For the ablation studies, we use a reduced set of 50 images. Detailed experiment setup is provided in [Appendix C.6](#). [Appendix D](#) provides additional visualizations.

Compute note. Our method has a tunable cost through the number of optimization steps, whereas DPS has a fixed cost once the diffusion chain length is set. Experiments below are meant to illustrate the effect of weak priors, not to provide a compute-matched benchmark. Thus, we report final reconstruction quality using each method’s default settings. [Appendix C.5](#) has a detailed discussion of compute and scaling, and includes additional experiments with strictly compute-matched settings that lead to the same conclusion.

4.1 Cross-Domain Inverse Problem Solving

Recall that weak priors can arise either from *(1) using a few-step sampler* or *(2) training on a mismatched dataset*. We therefore design the following cross-domain experiments to evaluate performance under both types of weak priors.

We consider four restoration tasks: inpainting, Gaussian deblurring, $4\times$ super-resolution, and nonlinear deblurring for bedroom, church, and human face images. For each task–dataset pair (e.g., human face inpainting), we benchmark reconstruction under a strong prior using the DPS algorithm [Chung et al. \(2023\)](#), which uses a 1000-step DDPM trained on the same distribution as the target image. We then compare against two weak-prior settings: a 3-step DDIM prior trained on matched dataset, and a 3-step DDIM prior trained on mismatched dataset (e.g., LSUN-Church or LSUN-Bedroom). For each weak prior, we solve the corresponding task using initial-noise optimization with our optimizer and `HOLDOUTTOPK` early-stopping strategy, as described in [Section 2.1](#). We choose a 3-step DDIM prior following the recommendation of [Wang et al. \(2024\)](#), which includes an ablation study over the number of DDIM steps.

[Table 2](#) reports results for inpainting and $4\times$ super-resolution, with the remaining tasks deferred to [Appendix C](#). The results suggest weak prior is able to achieve very efficient reconstructions. With initial-noise optimization, the few-step, in-domain prior overall outperforms the DPS baseline (which uses an in-domain, 1000-step prior) across all metrics. For example, our method achieves a PSNR gain of 0.88–1.80 dB on inpainting, and an even larger gain on super-resolution. These results are also consistent with [Wang et al. \(2024\)](#) and [Chihaoui et al. \(2024\)](#). Somewhat surprisingly, even with the weakest prior (out-of-domain and few-step generator), performance can still match or exceed DPS. For example, using a bedroom-pretrained model for CelebA inpainting, our method achieves

Table 2: Cross-Domain results for inpainting and super-resolution. The “Model” column indicates the source domain of the pretrained diffusion model. The “CelebA,” “Bedroom,” and “Church” columns indicate the target domains of the images being reconstructed. DPS always uses an in-domain model, i.e., the source and target domains coincide.

Task	Method	Model	CelebA			Bedroom			Church		
			PSNR \uparrow	LPIPS \downarrow	SSIM \uparrow	PSNR \uparrow	LPIPS \downarrow	SSIM \uparrow	PSNR \uparrow	LPIPS \downarrow	SSIM \uparrow
	DPS	In-domain	31.98	0.14	0.88	27.97	0.23	0.82	24.15	0.25	0.73
Inpainting	Ours	CelebA	33.78	0.15	0.91	27.78	0.27	0.83	23.56	0.36	0.72
		Bedroom	32.76	0.17	0.90	28.88	0.20	0.87	24.22	0.28	0.75
		Church	32.62	0.16	0.90	28.66	0.21	0.86	24.93	0.23	0.77
Super-Res	DPS	CelebA	26.82	0.22	0.74	22.95	0.39	0.64	20.28	0.36	0.52
	Ours	CelebA	31.27	0.18	0.86	25.88	0.35	0.74	22.68	0.41	0.63
		Bedroom	30.34	0.22	0.84	26.59	0.25	0.78	22.86	0.33	0.65
		Church	30.10	0.22	0.84	26.30	0.27	0.77	23.09	0.27	0.67

PSNR 32.76, compared to DPS’s 31.98. Thus, these results show that even few-step, out-of-domain diffusion generators can serve as effective priors.²

We also study how domain mismatch affects reconstruction quality. Specifically, we compare our method that use a few-step generator under matched versus mismatched source–target domains. As shown in Table 2, the in-domain generator outperforms the out-of-domain generator. The gap is sometimes moderate (e.g., CelebA inpainting) and sometimes small (e.g., Bedroom inpainting). Meanwhile, using a bedroom-trained model versus a church-trained model often yields similar performance, especially compared with CelebA-trained model. This matches the intuition that bedrooms and churches are more similar to each other than to human faces. These comparisons suggest that domain mismatch can affect performance, but the effect is often modest, smaller when the source and target domains are visually closer and larger when they are farther apart.

Table 3: Comparison with DMPlug under in-domain priors for random inpainting and nonlinear deblurring task.

Task	Dataset	Ours			DMPlug		
		PSNR \uparrow	LPIPS \downarrow	SSIM \uparrow	PSNR \uparrow	LPIPS \downarrow	SSIM \uparrow
Inpainting	CelebA	33.784	0.147	0.915	32.778	0.189	0.892
	Church	24.927	0.234	0.771	24.957	0.246	0.771
	Bedroom	28.883	0.201	0.867	28.271	0.255	0.836
Nonlinear	CelebA	25.21	0.27	0.74	24.85	0.28	0.73
	Church	20.88	0.39	0.56	20.48	0.42	0.53
	Bedroom	22.67	0.39	0.64	22.21	0.41	0.63

²Although our method generally outperforms DPS on these metrics, we do not intend to claim that a “weak prior” is strictly better than a “strong prior” in any general sense. The reason is that DPS is one of the most widely used strong-prior baselines, but it is not necessarily the best inverse-problem solver for every task and dataset. Nevertheless, consistently outperforming DPS provides strong evidence that weak, even out-of-domain priors can be practically effective in data-informative regimes.

4.2 Comparison with Optimization-Based Methods and Ablations

Next, we compare our method with the state-of-the-art optimization-based approach DMPlug [Wang et al. \(2024\)](#). Both methods optimize the initial noise, but with different optimizers and early-stopping strategies. To isolate the effect of algorithmic design, we use the same in-domain 3-step DDIM prior (as suggested in [Wang et al. \(2024\)](#)) and run both algorithms from the same randomly sampled initial noise, for the same number of iterations. Results for random inpainting and nonlinear deblurring are summarized in Table 3. Other tasks results are provided in Appendix C. Our PSNR exceeds DMPlug in most cases, with gains ranging from 0.15 to 1 dB; in the remaining cases, the difference is below 0.1 dB. Our LPIPS is consistently lower than DMPlug’s, with improvement up to 30%.

Table 4: PSNR for Gaussian denoising and inpainting. (A) Adam + variance, (B) Adam + HOLDOUTTOPK, (C) ADAMSPHERE + variance, (D) ADAMSPHERE + HOLDOUTTOPK.

Task	Dataset	(A)	(B)	(C)	(D)
Gaussian	Church	22.034	22.394	22.048	22.404
	Bedroom	24.825	25.595	24.854	25.596
Inpainting	Church	24.724	24.843	24.743	24.844
	Bedroom	28.669	29.156	28.559	29.162

We also include a small ablation study of our new optimizer, ADAMSPHERE, and our early-stopping strategy, HOLDOUTTOPK; the results are reported in Table 4. They indicate that ADAMSPHERE matches the optimization performance of standard Adam, while explicitly keeping the noise near the typical Gaussian shell, which has been found important for high-quality generation [Yang et al. \(2024\)](#); [Mannering et al. \(2025\)](#). Meanwhile, HOLDOUTTOPK consistently improves over the variance-based early-stopping baseline used in [Wang et al. \(2024\)](#). Thus, our strategy offers a simple, effective alternative for reducing overfitting.

4.3 Failure Modes

We examine the limitations of weak priors. To study this, we consider *box inpainting* and *large-scale super-resolution*, which are closer to generation than reconstruction. For example, box inpainting requires filling an entire region.

In both experiments, the goal is to recover church images. As before, DPS uses a full 1000-step DDPM prior trained on Church, while our method uses a 3-step DDIM prior trained on Church (in-domain) and on CelebA (out-of-domain), respectively. For box inpainting, we mask a contiguous square region whose size increases across trials,

and compare our method against the DPS baseline. Results are plotted in Figure 4 and recorded in Table 7 in Appendix C. We observe a clear failure mode: as the masked fraction increases, our method degrades and performs worse than DPS, with the performance gap growing as masking becomes more severe. In particular, the out-of-domain prior fails completely, as reflected in both the metrics and Figure 3 top row. The filled region has a face-like appearance that is clearly inconsistent with the church content. Similar observations appear for super-resolution. As the super-resolution factor increases, performance degrades sharply and essentially all methods fail. However, as shown in Figure 3 bottom row, DPS still generates higher-quality samples due to its stronger prior. In contrast, weak priors produce blurry, inconsistent samples.

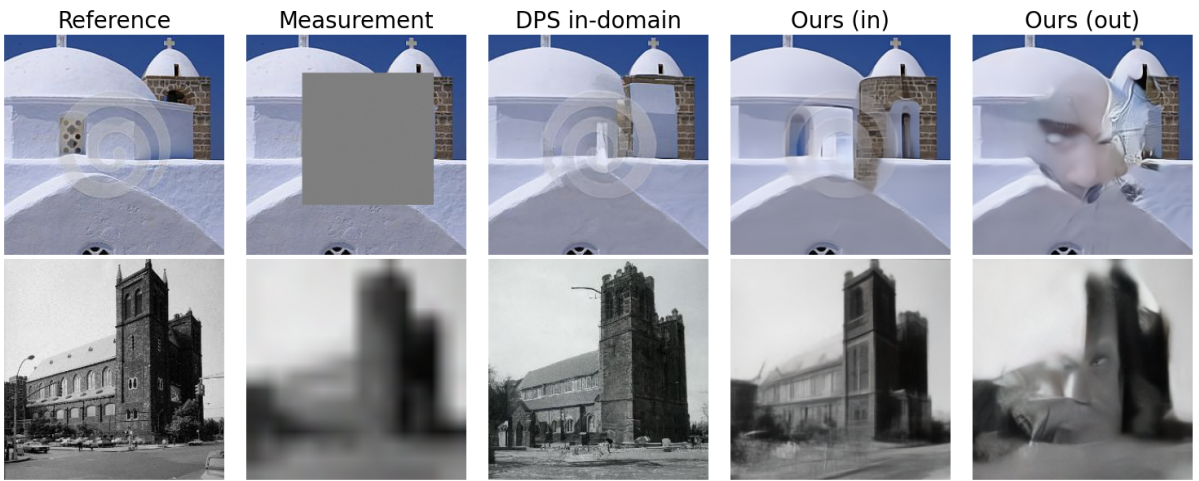


Figure 3: Visual comparison on box inpainting and super-resolution tasks. **Top row:** box inpainting with a 0.6×0.6 mask. **Bottom row:** $16 \times$ super-resolution.

4.4 Latent Diffusion Applications on ImageNet

To complement our previous experiments based on pixel-space diffusion models, we further evaluate our method using latent diffusion models on ImageNet. Motivated by the robust performance under prior mismatch observed in Section 4.1, we hypothesize that modern latent diffusion models (e.g., Stable Diffusion (SD) 2.1 [Rombach et al. \(2022\)](#) and DiT [Peebles & Xie \(2023\)](#)), trained on broad and diverse datasets, may serve as more general-purpose priors. We randomly sample 100 images from the ImageNet validation set [Deng et al. \(2009\)](#) and apply SD 2.1 and DiT priors. Results are reported in Table 8 in Appendix C. We find that these few-step latent diffusion generators, despite being weak priors, still yield accurate reconstructions.

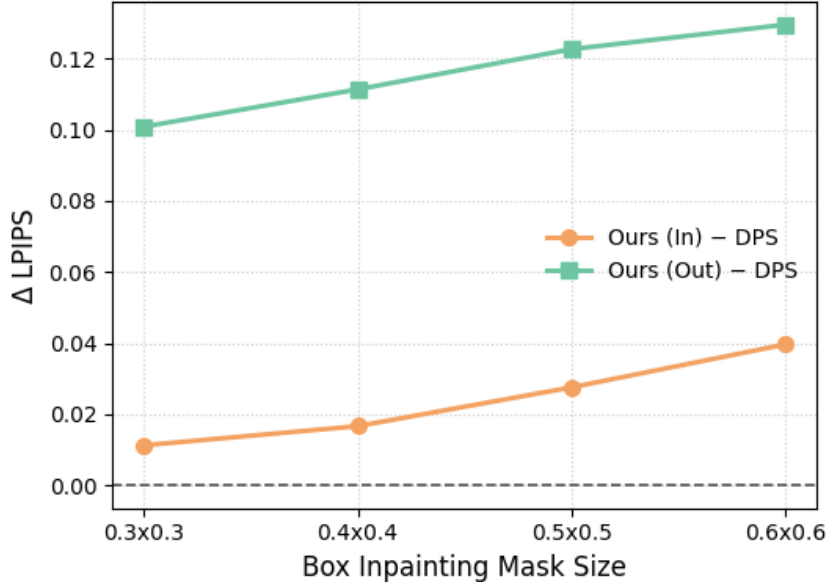


Figure 4: Difference in LPIPS between our method and the DPS baseline for different mask sizes. The dashed horizontal line denotes equal performance with DPS.

5 Conclusion and Discussion

This work studies when inverse-problem performance is robust to the choice of prior. We show that weak priors, arising either from low-fidelity generators or from training and reconstruction domain mismatch, can still perform well across many inverse problems. We support this finding with extensive empirical results. To explain this phenomenon, we develop new theory based on Bayesian consistency that connects measurement informativeness with reduced sensitivity to the prior. We prove that sufficiently informative measurements can effectively wash out the influence of a weak prior. Besides these success cases, we also characterize the regimes where failures occur.

Our results are encouraging conceptually and practically: when measurements are sufficiently informative, reconstruction is driven more by the observation than by the prior, so the prior may matter less than is often assumed. Therefore, practitioners can use weak priors as a reasonable default when well-matched strong priors are unavailable.

Looking forward, this phenomenon calls for further study of algorithms tailored to weak priors, especially few-step priors. Despite the strong performance of initial-noise optimization, existing work remains limited and largely centers on this single approach. Potential algorithmic improvements include hybrid methods that combine measurement injection (DPS-style) with noise optimization, improved early-stopping strategies, and more effective sampling procedures. Theoretically, while our theory explains both success and failure cases, further work is needed to pin down sharp thresholds that determine when measurements are informative enough for weak priors to be effective.

Acknowledgement

The authors thank Haochen Ji and Qian Qin for helpful discussions. Guanyang Wang and Jing Jia acknowledge support from the National Science Foundation through grant DMS-2210849 and an Adobe Data Science Research Award. Liyue Shen acknowledges funding support by NSF (National Science Foundation) via grants IIS-2435746, Defense Advanced Research Projects Agency (DARPA) under Contract No. HR00112520042, Hyundai America Technical Center, Inc. (HATCI), as well as the University of Michigan MICDE Catalyst Grant Award and MIDAS PODS Grant Award.

References

Aali, A., Daras, G., Levac, B., Kumar, S., Dimakis, A. G., and Tamir, J. I. Ambient diffusion posterior sampling: Solving inverse problems with diffusion models trained on corrupted data. *arXiv preprint arXiv:2403.08728*, 2024.

Barbano, R., Denker, A., Chung, H., Roh, T. H., Arridge, S., Maass, P., Jin, B., and Ye, J. C. Steerable conditional diffusion for out-of-distribution adaptation in medical image reconstruction. *IEEE Transactions on Medical Imaging*, 2025.

Bardenet, R. and Maillard, O.-A. Concentration inequalities for sampling without replacement. *Bernoulli*, 21(3):1361–1385, 2015.

Ben-Hamu, H., Puny, O., Gat, I., Karrer, B., Singer, U., and Lipman, Y. D-flow: Differentiating through flows for controlled generation. In *International Conference on Machine Learning*, pp. 3462–3483. PMLR, 2024.

Bora, A., Jalal, A., Price, E., and Dimakis, A. G. Compressed sensing using generative models. In *International conference on machine learning*, pp. 537–546. PMLR, 2017.

Chihaoui, H., Lemkhenter, A., and Favaro, P. Blind image restoration via fast diffusion inversion. *Advances in Neural Information Processing Systems*, 37:34513–34532, 2024.

Chung, H., Kim, J., Mccann, M. T., Klasky, M. L., and Ye, J. C. Diffusion posterior sampling for general noisy inverse problems. In *The Eleventh International Conference on Learning Representations*, 2023. URL <https://openreview.net/forum?id=OnD9zGAGT0k>.

Deng, J., Dong, W., Socher, R., Li, L.-J., Li, K., and Fei-Fei, L. Imagenet: A large-scale hierarchical image database. In *2009 IEEE conference on computer vision and pattern recognition*, pp. 248–255. Ieee, 2009.

Gatmiry, K., Kelner, J., and Lee, H. Learning mixtures of gaussians using diffusion models. *arXiv preprint arXiv:2404.18869*, 2024.

Ghosal, S. and Van der Vaart, A. W. *Fundamentals of nonparametric Bayesian inference*, volume 44. Cambridge University Press, 2017.

Glaszner, L. and Zach, M. Bigger isn't always better: Towards a general prior for medical image reconstruction. In *DAGM German Conference on Pattern Recognition*, pp. 275–291. Springer, 2024.

Ho, J., Jain, A., and Abbeel, P. Denoising diffusion probabilistic models. *Advances in neural information processing systems*, 33:6840–6851, 2020.

Hoeffding, W. Probability inequalities for sums of bounded random variables. *Journal of the American statistical association*, 58(301):13–30, 1963.

Hu, J., Song, B., Fessler, J. A., and Shen, L. Test-time adaptation improves inverse problem solving with patch-based diffusion models. *IEEE Transactions on Computational Imaging*, 2025.

Jalal, A., Arvinte, M., Daras, G., Price, E., Dimakis, A. G., and Tamir, J. Robust compressed sensing mri with deep generative priors. *Advances in neural information processing systems*, 34:14938–14954, 2021.

Jia, J., Liu, S., Song, B., Yuan, W., Shen, L., and Wang, G. Antithetic noise in diffusion models. *arXiv preprint arXiv:2506.06185*, 2025.

Karras, T., Laine, S., and Aila, T. A style-based generator architecture for generative adversarial networks. In *Proceedings of the IEEE/CVF conference on computer vision and pattern recognition*, pp. 4401–4410, 2019.

Kawar, B., Elad, M., Ermon, S., and Song, J. Denoising diffusion restoration models. *Advances in neural information processing systems*, 35:23593–23606, 2022.

Knoll, F., Hammernik, K., Kobler, E., Pock, T., Recht, M. P., and Sodickson, D. K. Assessment of the generalization of learned image reconstruction and the potential for transfer learning. *Magnetic resonance in medicine*, 81(1):116–128, 2019.

Liang, Y., Sha, Z., Shi, Z., Song, Z., Wan, M., and Zhou, Y. Unraveling the smoothness properties of diffusion models: A gaussian mixture perspective. In *Proceedings of the IEEE/CVF International Conference on Computer Vision*, pp. 11436–11446, 2025.

Liu, Z., Luo, P., Wang, X., and Tang, X. Deep learning face attributes in the wild. In *Proceedings of International Conference on Computer Vision (ICCV)*, December 2015.

Ma, N., Tong, S., Jia, H., Hu, H., Su, Y.-C., Zhang, M., Yang, X., Li, Y., Jaakkola, T., Jia, X., et al. Scaling inference time compute for diffusion models. In *Proceedings of the Computer Vision and Pattern Recognition Conference*, pp. 2523–2534, 2025.

Mannering, H., Huang, Z., and Prugel-Bennett, A. Noise-level diffusion guidance: Well begun is half done. *arXiv preprint arXiv:2509.13936*, 2025.

McLachlan, G. J. and Peel, D. *Finite mixture models*. John Wiley & Sons, 2000.

Meng, X. and Kabashima, Y. Diffusion model based posterior sampling for noisy linear inverse problems. *arXiv preprint arXiv:2211.12343*, 2022.

Peebles, W. and Xie, S. Scalable diffusion models with transformers. In *Proceedings of the IEEE/CVF international conference on computer vision*, pp. 4195–4205, 2023.

Rombach, R., Blattmann, A., Lorenz, D., Esser, P., and Ommer, B. High-resolution image synthesis with latent diffusion models. In *Proceedings of the IEEE/CVF conference on computer vision and pattern recognition*, pp. 10684–10695, 2022.

Schwartz, L. On Bayes procedures. *Zeitschrift für Wahrscheinlichkeitstheorie und verwandte Gebiete*, 4(1):10–26, 1965.

Shah, K., Chen, S., and Klivans, A. Learning mixtures of gaussians using the ddpm objective. *Advances in Neural Information Processing Systems*, 36:19636–19649, 2023.

Song, B., Kwon, S. M., Zhang, Z., Hu, X., Qu, Q., and Shen, L. Solving inverse problems with latent diffusion models via hard data consistency. In *The Twelfth International Conference on Learning Representations*, 2024. URL <https://openreview.net/forum?id=j8hdRqOUhN>.

Song, J., Meng, C., and Ermon, S. Denoising diffusion implicit models. In *International Conference on Learning Representations*, 2021a. URL <https://openreview.net/forum?id=St1giarCHLP>.

Song, Y., Sohl-Dickstein, J., Kingma, D. P., Kumar, A., Ermon, S., and Poole, B. Score-based generative modeling through stochastic differential equations. In *International Conference on Learning Representations*, 2021b. URL <https://openreview.net/forum?id=PxTIG12RRHS>.

Song, Y., Shen, L., Xing, L., and Ermon, S. Solving inverse problems in medical imaging with score-based generative models. In *International Conference on Learning Representations*, 2022. URL <https://openreview.net/forum?id=vaRCHVj0uGI>.

Tang, Z., Peng, J., Tang, J., Hong, M., Wang, F., and Chang, T.-H. Inference-time alignment of diffusion models with direct noise optimization. In *Forty-second International Conference on Machine Learning*, 2025. URL <https://openreview.net/forum?id=JpbqiD7n9r>.

Tran, P., Tran, A., Phung, Q., and Hoai, M. Explore image deblurring via encoded blur kernel space. In *Proceedings of the IEEE Conference on Computer Vision and Pattern Recognition (CVPR)*, 2021.

Vershynin, R. *High-dimensional probability: An introduction with applications in data science*, volume 47. Cambridge university press, 2018.

Wan, Y., Devera, R., Zhang, W., and Sun, J. Fmplug: Plug-in foundation flow-matching priors for inverse problems. *arXiv preprint arXiv:2508.00721*, 2025.

Wang, H., Zhang, X., Li, T., Wan, Y., Chen, T., and Sun, J. Dmplug: A plug-in method for solving inverse problems with diffusion models. *Advances in Neural Information Processing Systems*, 37:117881–117916, 2024.

Wu, Y., Chen, M., Li, Z., Wang, M., and Wei, Y. Theoretical insights for diffusion guidance: a case study for gaussian mixture models. In *Proceedings of the 41st International Conference on Machine Learning*, pp. 53291–53327, 2024.

Yang, L., Ding, S., Cai, Y., Yu, J., Wang, J., and Shi, Y. Guidance with spherical gaussian constraint for conditional diffusion. In *International Conference on Machine Learning*, pp. 56071–56095. PMLR, 2024.

Yu, F., Seff, A., Zhang, Y., Song, S., Funkhouser, T., and Xiao, J. Lsun: Construction of a large-scale image dataset using deep learning with humans in the loop. *arXiv preprint arXiv:1506.03365*, 2015.

Zhang, R., Isola, P., Efros, A. A., Shechtman, E., and Wang, O. The unreasonable effectiveness of deep features as a perceptual metric. In *Proceedings of the IEEE conference on computer vision and pattern recognition*, pp. 586–595, 2018.

Zheng, H., Chu, W., Zhang, B., Wu, Z., Wang, A., Feng, B., Zou, C., Sun, Y., Kovachki, N. B., Ross, Z. E., Bouman, K., and Yue, Y. Inversebench: Benchmarking Plug-and-Play Diffusion Priors for Inverse Problems in Physical Sciences. In

The Thirteenth International Conference on Learning Representations, 2025. URL <https://openreview.net/forum?id=U3PBITXNG6>.

Zhou, S., Zhu, H., Sharma, R., Chen, J., Zhang, R., Ji, K., and Chen, C. Enhancing diffusion posterior sampling for inverse problems by integrating crafted measurements. *arXiv preprint arXiv:2411.09850*, 2024.

Zhou, Z., Shao, S., Bai, L., Zhang, S., Xu, Z., Han, B., and Xie, Z. Golden noise for diffusion models: A learning framework. In *Proceedings of the IEEE/CVF International Conference on Computer Vision*, pp. 17688–17697, 2025.

A Additional theoretical results and proofs

A.1 Posterior consistency under i.i.d. data

The following theorem gives posterior consistency for i.i.d. data. It goes back to [Schwartz \(1965\)](#); see also Chapter 6 of [Ghosal & Van der Vaart \(2017\)](#) for extensions.

Theorem A.1 (Posterior consistency). *Let (\mathcal{X}, d) be a metric space and let $\{P_x\}_{x \in \mathcal{X}}$ be a dominated i.i.d. model: there exists a σ -finite measure μ such that $P_x \ll \mu$ with density $p_x = \frac{dP_x}{d\mu}$ for every $x \in \mathcal{X}$. Let Y_1, Y_2, \dots be i.i.d. from P_{x^*} , and let π be a prior on \mathcal{X} . Write $Y_{1:n} = (Y_1, \dots, Y_n)$ and*

$$\pi(A \mid Y_{1:n}) = \frac{\int_A \prod_{i=1}^n p_x(Y_i) \pi(dx)}{\int_{\mathcal{X}} \prod_{i=1}^n p_x(Y_i) \pi(dx)}.$$

Assume:

(i) **KL support at the truth:** for every $\varepsilon > 0$,

$$\pi(\{x \in \mathcal{X} : \text{KL}(P_{x^*}, P_x) < \varepsilon\}) > 0, \quad \text{KL}(P_{x^*}, P_x) := \int \log\left(\frac{p_{x^*}}{p_x}\right) dP_{x^*},$$

where **KL** stands for the Kullback-Leibler (KL) divergence.

(ii) **Existence of uniformly consistent tests:** for every $\delta > 0$ there exists a sequence of tests $\phi_n = \phi_n(Y_{1:n}) \in [0, 1]$ such that

$$\mathbb{E}_{x^*}[\phi_n] \rightarrow 0 \quad \text{and} \quad \sup_{x: d(x, x^*) > \delta} \mathbb{E}_x[1 - \phi_n] \rightarrow 0 \quad \text{as } n \rightarrow \infty.$$

Then the posterior is (strongly) consistent at x^* : for every $\delta > 0$,

$$\pi(\{x \in \mathcal{X} : d(x, x^*) > \delta\} \mid Y_{1:n}) \rightarrow 0 \quad \text{almost surely under } P_{x^*}^\infty.$$

A.2 Close-formula for Gaussian mixture posterior

Proposition A.2. *Given the measurement model $y = Ax + \epsilon$, where $\epsilon \sim \mathbb{N}(0, \sigma^2 I_m)$, and a Gaussian mixture prior*

$$\pi(x) = \sum_{j=1}^M w_j \varphi(x; \mu_j, \Sigma_j), \quad w_j \geq 0, \quad \sum_{j=1}^M w_j = 1,$$

where each $\Sigma_j \in \mathbb{R}^{n \times n}$ is symmetric positive definite. Then the posterior $\pi(x \mid y)$ is also a Gaussian mixture:

$$\pi(x \mid y) = \sum_{j=1}^M \tilde{w}_j(y) \varphi(x; m_j(y), C_j),$$

where,

$$C_j := \left(\Sigma_j^{-1} + \frac{1}{\sigma^2} A^\top A \right)^{-1},$$

$$m_j(y) := C_j \left(\Sigma_j^{-1} \mu_j + \frac{1}{\sigma^2} A^\top y \right).$$

The updated weights satisfy

$$\tilde{w}_j(y) = \frac{w_j \varphi(y; A\mu_j, \sigma^2 I_m + A\Sigma_j A^\top)}{\sum_{\ell=1}^M w_\ell \varphi(y; A\mu_\ell, \sigma^2 I_m + A\Sigma_\ell A^\top)}.$$

Proof. The posterior density

$$\pi(x \mid y) = \frac{p(y \mid x) \pi(x)}{\int p(y \mid x) \pi(x) dx} = \frac{\sum_{j=1}^M w_j \varphi(y; Ax, \sigma^2 I_m) \varphi(x; \mu_j, \Sigma_j)}{\sum_{j=1}^M w_j \int \varphi(y; Ax, \sigma^2 I_m) \varphi(x; \mu_j, \Sigma_j) dx}.$$

Thus it suffices to analyze, for each fixed j , the product

$$\varphi(y; Ax, \sigma^2 I_m) \varphi(x; \mu_j, \Sigma_j).$$

Fix j . Consider the hierarchical model

$$X \sim \mathbb{N}(\mu_j, \Sigma_j), \quad Y \mid X = x \sim \mathbb{N}(Ax, \sigma^2 I_m).$$

It is known that (X, Y) is jointly Gaussian with mean $(\mu_j, A\mu_j)$ and covariance

$$\begin{pmatrix} \Sigma_j & \Sigma_j A^\top \\ A\Sigma_j & A\Sigma_j A^\top + \sigma^2 I_m \end{pmatrix}.$$

In particular, the marginal distribution of Y under component j is

$$p_j(y) := \int \varphi(y; Ax, \sigma^2 I_m) \varphi(x; \mu_j, \Sigma_j) dx = \varphi(y; A\mu_j, \sigma^2 I_m + A\Sigma_j A^\top).$$

Also, the conditional distribution of X given $Y = y$ under component j is Gaussian with covariance

$$\tilde{C}_j = \Sigma_j - \Sigma_j A^\top \left(\sigma^2 I_m + A\Sigma_j A^\top \right)^{-1} A\Sigma_j$$

and mean

$$\tilde{m}_j(y) = \mu_j + \Sigma_j A^\top \left(\sigma^2 I_m + A\Sigma_j A^\top \right)^{-1} (y - A\mu_j).$$

Using the Woodbury identity, one can check that

$$\tilde{C}_j = \left(\Sigma_j^{-1} + \frac{1}{\sigma^2} A^\top A \right)^{-1} =: C_j,$$

and substituting this into the expression for $\tilde{m}_j(y)$ gives the equivalent form

$$\tilde{m}_j(y) = C_j \left(\Sigma_j^{-1} \mu_j + \frac{1}{\sigma^2} A^\top y \right) =: m_j(y).$$

Therefore, for each j we have the factorization of the joint density

$$\varphi(y; Ax, \sigma^2 I_m) \varphi(x; \mu_j, \Sigma_j) = p_j(y) \varphi(x; m_j(y), C_j),$$

where $p_j(y) = \varphi(y; A\mu_j, \sigma^2 I_m + A\Sigma_j A^\top)$.

Plugging this into Bayes' rule yields

$$\pi(x \mid y) = \frac{\sum_{j=1}^M w_j p_j(y) \varphi(x; m_j(y), C_j)}{\sum_{\ell=1}^M w_\ell p_\ell(y)} = \sum_{j=1}^M \tilde{w}_j(y) \varphi(x; m_j(y), C_j),$$

with

$$\tilde{w}_j(y) = \frac{w_j p_j(y)}{\sum_{\ell=1}^M w_\ell p_\ell(y)} = \frac{w_j \varphi(y; A\mu_j, \sigma^2 I_m + A\Sigma_j A^\top)}{\sum_{\ell=1}^M w_\ell \varphi(y; A\mu_\ell, \sigma^2 I_m + A\Sigma_\ell A^\top)}.$$

This is exactly the stated Gaussian-mixture posterior with the given component means, covariances, and updated weights.

□

A.3 Posterior collapse under heterogeneous variances

Here we prove a more general version of Theorem 3.2 under a heterogeneous-variance assumption.

Setup: Consider the measurement model

$$y = Ax + \epsilon, \quad \epsilon \sim \mathbb{N}(0, \sigma^2 I_m),$$

and the Gaussian mixture

$$\pi(x) = \sum_{j=1}^M w_j \varphi(x; \mu_j, \tau_j^2 I_n), \quad w_j \geq 0, \quad \sum_{j=1}^M w_j = 1.$$

We note that this setting is strictly more general than the equal-variance setting in our main text (3), since each component is allowed to have its own covariance scale $\tau_j^2 I_n$.

It reduces to the homogeneous case when $\tau_1 = \tau_2 = \dots = \tau_M = \tau$.

We prove the following theorem:

Theorem A.3 (Posterior collapse to the best *selection-score* mode). *Consider the measurement model and Gaussian mixture prior as above. Let*

$$\Sigma_j := \sigma^2 I_m + \tau_j^2 A A^\top.$$

Define the selection score

$$\ell_j(y^*) := s_j(y^*) + \frac{1}{2} \log \det(\Sigma_j), \quad s_j(y^*) := \frac{1}{2} \left\| \Sigma_j^{-1/2} (y^* - A\mu_j) \right\|_2^2. \quad (6)$$

Let $\ell_{(1)}(y^*)$ and $\ell_{(2)}(y^*)$ be the smallest and second-smallest values among $\{\ell_j(y^*)\}_{j=1}^M$, and define the per-dimension selection-score gap

$$\delta_\ell(y^*) := \frac{1}{m} \left(\ell_{(2)}(y^*) - \ell_{(1)}(y^*) \right). \quad (7)$$

Assume:

1. (Bounded weight ratio) There exists $C > 1$ such that $1/C \leq w_i/w_j \leq C$ for all i, j .
2. (δ_0 -identifiable in selection score) There is a unique minimizer

$$j^* = \arg \min_{1 \leq j \leq M} \ell_j(y^*),$$

and $\delta_\ell(y^*) \geq \delta_0$ for some constant $\delta_0 > 0$.

Let J be the posterior component index, i.e.

$$\Pr(J = j) = \tilde{w}_j(y^*) := \frac{w_j \varphi(y^*; A\mu_j, \Sigma_j)}{\sum_{i=1}^M w_i \varphi(y^*; A\mu_i, \Sigma_i)}.$$

Then

- The probability of not selecting the best selection-score component satisfies

$$\Pr(J \neq j^*) \leq CM e^{-m\delta_0}.$$

- The posterior concentrates onto the j^* -th Gaussian component at an exponential rate:

$$\left\| \pi(\cdot | y^*) - \mathbb{N}(m_{j^*}(y^*), \Sigma_{\text{post}, j^*}) \right\|_{\text{TV}} \leq CM e^{-m\delta_0},$$

where

$$\Sigma_{\text{post},j} = \left(\tau_j^{-2} I_n + \frac{1}{\sigma^2} A^\top A \right)^{-1}, \quad m_j(y^*) = \Sigma_{\text{post},j} \left(\tau_j^{-2} \mu_j + \frac{1}{\sigma^2} A^\top y^* \right).$$

Remark A.4. Theorem A.3 reduces to Theorem 3.2 when $\tau_1 = \dots = \tau_M = \tau$.

Proof. By Proposition A.2, the posterior weights satisfy

$$\tilde{w}_j(y^*) \propto w_j \varphi(y^*; A\mu_j, \Sigma_j), \quad \Sigma_j = \sigma^2 I_m + \tau_j^2 A A^\top.$$

Fix $j \neq j^*$. Using the Gaussian density formula,

$$\begin{aligned} \frac{\tilde{w}_j(y^*)}{\tilde{w}_{j^*}(y^*)} &= \frac{w_j}{w_{j^*}} \frac{\varphi(y^*; A\mu_j, \Sigma_j)}{\varphi(y^*; A\mu_{j^*}, \Sigma_{j^*})} \\ &= \frac{w_j}{w_{j^*}} \left(\frac{\det(\Sigma_{j^*})}{\det(\Sigma_j)} \right)^{1/2} \exp \left(-s_j(y^*) + s_{j^*}(y^*) \right) \\ &= \frac{w_j}{w_{j^*}} \exp \left(-[s_j(y^*) + \frac{1}{2} \log \det(\Sigma_j)] + [s_{j^*}(y^*) + \frac{1}{2} \log \det(\Sigma_{j^*})] \right) \\ &= \frac{w_j}{w_{j^*}} \exp \left(-(\ell_j(y^*) - \ell_{j^*}(y^*)) \right). \end{aligned} \tag{8}$$

By the bounded weight-ratio assumption, $w_j/w_{j^*} \leq C$ for all j , hence

$$\frac{\tilde{w}_j(y^*)}{\tilde{w}_{j^*}(y^*)} \leq C \exp \left(-(\ell_j(y^*) - \ell_{j^*}(y^*)) \right). \tag{9}$$

Next, note that

$$\Pr(J \neq j^*) = \sum_{j \neq j^*} \tilde{w}_j(y^*) = \tilde{w}_{j^*}(y^*) \sum_{j \neq j^*} \frac{\tilde{w}_j(y^*)}{\tilde{w}_{j^*}(y^*)} \leq \sum_{j \neq j^*} \frac{\tilde{w}_j(y^*)}{\tilde{w}_{j^*}(y^*)},$$

since $\tilde{w}_{j^*}(y^*) \leq 1$. Combining with (9) gives

$$\Pr(J \neq j^*) \leq C \sum_{j \neq j^*} \exp \left(-(\ell_j(y^*) - \ell_{j^*}(y^*)) \right).$$

By definition of $\ell_{(2)}$ and $\ell_{(1)} = \ell_{j^*}$, we have $\ell_j(y^*) - \ell_{j^*}(y^*) \geq \ell_{(2)}(y^*) - \ell_{(1)}(y^*)$ for all $j \neq j^*$. Therefore,

$$\Pr(J \neq j^*) \leq C(M-1) \exp \left(-(\ell_{(2)}(y^*) - \ell_{(1)}(y^*)) \right) \leq CM \exp(-m\delta_\ell(y^*)) \leq CM \exp(-m\delta_0),$$

which proves the first claim.

For the total-variation bound, write the posterior mixture as

$$\pi(\cdot | y^*) = \tilde{w}_{j^*}(y^*) \mathbb{N}(m_{j^*}(y^*), \Sigma_{\text{post},j^*}) + \sum_{j \neq j^*} \tilde{w}_j(y^*) \mathbb{N}(m_j(y^*), \Sigma_{\text{post},j}).$$

Let $\mu^* := \mathbb{N}(m_{j^*}(y^*), \Sigma_{\text{post},j^*})$. Then, using that $\|\nu_1 - \nu_2\|_{\text{TV}} \leq 1$ for any probability measures ν_1, ν_2 ,

$$\|\pi(\cdot | y^*) - \mu^*\|_{\text{TV}} = \left\| \sum_{j \neq j^*} \tilde{w}_j(y^*) (\mathbb{N}(m_j, \Sigma_{\text{post},j}) - \mu^*) \right\|_{\text{TV}} \leq \sum_{j \neq j^*} \tilde{w}_j(y^*) \|\mathbb{N}(m_j, \Sigma_{\text{post},j}) - \mu^*\|_{\text{TV}} \leq \sum_{j \neq j^*} \tilde{w}_j(y^*)$$

Hence

$$\|\pi(\cdot | y^*) - \mu^*\|_{\text{TV}} \leq \Pr(J \neq j^*) \leq C M e^{-m\delta_0},$$

as claimed. \square

A.4 Validating Assumption 2 in Theorem 3.2

We give a simple probabilistic argument showing that the δ_0 -identifiable condition in Assumption 2 holds with high probability for *random inpainting*, provided the candidate means are separated in full-image MSE.

Setup. Let $A = P_\Omega$ be a coordinate projection onto a uniformly random subset $\Omega \subset [n]$ with $|\Omega| = m$. Assume all pixel values are bounded: $|\mu_{j,i}| \leq 1$ for all j, i . Consider the Gaussian-mixture surrogate where the data are generated from a single component j^* :

$$x^* = \mu_{j^*} + \xi, \quad \xi \sim \mathbb{N}(0, \tau^2 I_n), \quad y^* = P_\Omega x^* + \epsilon, \quad \epsilon \sim \mathbb{N}(0, \sigma^2 I_m),$$

so that

$$y^* = P_\Omega \mu_{j^*} + \eta, \quad \eta := P_\Omega \xi + \epsilon \sim \mathbb{N}(0, (\sigma^2 + \tau^2) I_m).$$

Recall that for inpainting,

$$s_j(y^*) = \frac{1}{2(\sigma^2 + \tau^2)} \|y^* - P_\Omega \mu_j\|_2^2.$$

Assume there exists $\Delta > 0$ such that for every $j \neq j^*$,

$$\frac{1}{n} \|\mu_j - \mu_{j^*}\|_2^2 \geq \Delta. \quad (10)$$

This is a full-image (population) MSE separation between the correct mean and all others, which is natural because visually different images typically differ across many pixels.

Then we show the following:

Proposition A.5 (Identifiability for random inpainting). *Under the setup above and (10), define the per-dimension score gap*

$$\delta(y^*) := \min_{j \neq j^*} \frac{s_j(y^*) - s_{j^*}(y^*)}{m}.$$

Then there is a universal constant $c > 0$ such that

$$\mathbb{P}\left(\delta(y^*) \geq \frac{\Delta}{8(\sigma^2 + \tau^2)}\right) \geq 1 - 2(M-1)\exp\left(-\frac{1}{32}m\Delta^2\right) - 2(M-1)\exp\left(-\frac{m\Delta^2}{32(\sigma^2 + \tau^2)}\right).$$

In other words, the score will be $\frac{\Delta}{8(\sigma^2 + \tau^2)}$ -identifiable with probability tending to 1 exponentially fast in m .

Proof. We pick an arbitrary $j \neq j^*$, write

$$y^* - P_\Omega \mu_j = P_\Omega(\mu_{j^*} - \mu_j) + \eta.$$

Therefore $y^* - P_\Omega \mu_j \sim \mathbb{N}(P_\Omega(\mu_{j^*} - \mu_j), (\sigma^2 + \tau^2)I_m)$. Let $v_j := P_\Omega(\mu_{j^*} - \mu_j)$. Expanding and cancelling the common $\|\eta\|_2^2$ term gives

$$\begin{aligned} s_j(y^*) - s_{j^*}(y^*) &= \frac{1}{2(\sigma^2 + \tau^2)} \left(\|v_j + \eta\|_2^2 - \|\eta\|_2^2 \right) \\ &= \frac{1}{2(\sigma^2 + \tau^2)} \left(\|v_j\|_2^2 + 2\langle \eta, v_j \rangle \right). \end{aligned}$$

Dividing by m , we have

$$\frac{s_j(y^*) - s_{j^*}(y^*)}{m} = \frac{1}{2(\sigma^2 + \tau^2)} \left(\frac{1}{m} \|v_j\|_2^2 + \frac{2}{m} \langle \eta, v_j \rangle \right). \quad (11)$$

Therefore,

$$\mathbb{P}\left(\frac{s_j(y^*) - s_{j^*}(y^*)}{m} \geq \frac{\Delta}{8(\sigma^2 + \tau^2)}\right) = \mathbb{P}\left(\left(\frac{1}{m} \|v_j\|_2^2 + \frac{2}{m} \langle \eta, v_j \rangle\right) \geq \frac{\Delta}{4}\right)$$

We first bound the mask term $\frac{1}{m} \|v_j\|_2^2$. Define the population average

$$d_j := \frac{1}{n} \|\mu_{j^*} - \mu_j\|_2^2, \quad \hat{d}_j := \frac{1}{m} \|P_\Omega(\mu_{j^*} - \mu_j)\|_2^2 = \frac{1}{m} \|v_j\|_2^2.$$

Each summand $(\mu_{j^*,i} - \mu_{j,i})^2$ lies in $[0, 4]$. Since Ω is a uniform sample without replacement, Hoeffding's inequality (sampling without replace version, see Hoeffding (1963) or

Proposition 1.2 of [Bardenet & Maillard \(2015\)](#)) yields, for any $t > 0$,

$$\mathbb{P}(|\hat{d}_j - d_j| \geq t) \leq 2 \exp\left(-\frac{mt^2}{8}\right).$$

Taking $t = \Delta/2$ and using $d_j \geq \Delta$ from (10) gives

$$\mathbb{P}(\hat{d}_j \leq \Delta/2) \leq 2 \exp\left(-\frac{m\Delta^2}{32}\right).$$

Now we bound the noise term. Conditional on Ω , $\langle \eta, v_j \rangle$ is Gaussian with mean 0 and variance $(\sigma^2 + \tau^2)\|v_j\|_2^2$. Hence, for any $a > 0$, the classical Gaussian concentration bound implies

$$\mathbb{P}\left(\left|\frac{2}{m}\langle \eta, v_j \rangle\right| \geq a \mid \Omega\right) \leq 2 \exp\left(-\frac{m^2 a^2}{8(\sigma^2 + \tau^2)\|v_j\|_2^2}\right).$$

Using the coordinate bound $|\langle \mu_{j^*,i} - \mu_{j,i} \rangle| \leq 2$ gives $\|v_j\|_2^2 \leq 4m$, so

$$\mathbb{P}\left(\left|\frac{2}{m}\langle \eta, v_j \rangle\right| \geq a \mid \Omega\right) \leq 2 \exp\left(-\frac{ma^2}{32(\sigma^2 + \tau^2)}\right).$$

Taking $a = \Delta/4$, on the event $\{\hat{d}_j \geq \Delta/2\}$ and $\left\{\left|\frac{2}{m}\langle \eta, v_j \rangle\right| \leq \Delta/4\right\}$, the quantity

$$\frac{1}{m}\|v_j\|_2^2 + \frac{2}{m}\langle \eta, v_j \rangle$$

in (11) is at least $\Delta/4$, so

$$\mathbb{P}\left(\left(\frac{1}{m}\|v_j\|_2^2 + \frac{2}{m}\langle \eta, v_j \rangle\right) \geq \frac{\Delta}{4}\right) \geq 1 - 2 \exp\left(-\frac{m\Delta^2}{32}\right) - 2 \exp\left(-\frac{ma^2}{32(\sigma^2 + \tau^2)}\right).$$

A union bound over $j \neq j^*$ completes the proof. □

B Details of AdamSphere and HoldoutTopK

AdamSphere optimizer. When optimizing the initial noise variable z in diffusion-based inverse problems, we enforce the spherical constraint $\|z\|_2 = r$ (with r fixed, or set to $\|z^{(0)}\|_2$ at initialization). This prevents the optimizer from trivially changing the noise magnitude and keeps the search within the typical set of the Gaussian prior. ADAMSPHERE optimizer adapts Adam to this constraint: at each iteration, we first project the Euclidean gradient onto the tangent space of the sphere at the current iterate, apply Adam's moment updates using this tangent gradient, and then project the preconditioned

search direction back to the tangent space. Finally, we take a step along this tangent direction and retract back to the sphere. We use the simple normalization retraction by default (rescale the updated vector to norm r), and also consider an exponential-map retraction that moves along a great circle on the sphere.

HoldoutTopK early stopping. When optimizing the initial noise, later iterates can begin to overfit the observed pixels: the measurement error keeps decreasing, but visual quality (or metrics such as PSNR/LPIPS) may deteriorate. To avoid overfitting, we use a simple holdout-based early-stopping rule, `HOLDOUTTOPK`. We randomly split the observed index set Ω into a *fit* subset Ω_{fit} used for optimization and a disjoint *holdout* subset Ω_{ho} that is never used in gradient updates. At each iteration t , we evaluate a holdout score (e.g., the MSE on Ω_{ho}) and keep the K iterates with the lowest holdout scores. We then output an iterate chosen from this top- K set (e.g., the best within the top- K , or uniformly at random among them).

Our idea is inspired by standard practice in statistical machine learning, where a validation set is used to approximate test performance and guide model selection. However, unlike standard model selection that picks the single lowest-error candidate, we keep the top- K lowest-error iterates and eventually return the latest iterate among these top K . Using $K > 1$ stabilizes selection by avoiding the risk of picking a single spurious “best” iterate due to holdout noise, while still favoring iterates that consistently generalize well to unseen pixels. In practice, `HOLDOUTTOPK` provides a lightweight and robust way to reduce overfitting.

C Additional experiment results and experiment details

C.1 Cross-Domain Inverse Problem Solving

Table 5 presents additional cross-domain results for Gaussian and nonlinear deblurring. Consistent with Section 4.1, these experiments further confirm that a weak diffusion prior, such as a few-step or domain-mismatched one, remains highly competitive with the DPS baseline. For Gaussian deblurring, DPS performs well in-domain, but our method frequently surpasses it in PSNR and SSIM despite using substantially weaker priors. With the more challenging nonlinear deblurring task, the same qualitative conclusions hold and further demonstrate that weak priors are effective and robust for inverse problems.

Table 5: Cross-Domain results for Gaussian deblurring and nonlinear deblurring measurements. The “Model” column indicates the source domain of the pretrained diffusion model. The “CelebA,” “Bedroom,” and “Church” columns indicate the target domain of the images being reconstructed. DPS always uses an in-domain model, i.e., the source and target domains coincide.

Task	Method	Model	CelebA			Bedroom			Church		
			PSNR ↑	LPIPS ↓	SSIM ↑	PSNR ↑	LPIPS ↓	SSIM ↑	PSNR ↑	LPIPS ↓	SSIM ↑
Gaussian	DPS	In-domain	27.55	0.19	0.76	23.94	0.31	0.67	20.66	0.30	0.55
		CelebA	29.98	0.21	0.82	25.02	0.41	0.69	22.21	0.45	0.58
	Ours	Bedroom	27.97	0.27	0.77	25.28	0.30	0.72	22.09	0.38	0.59
Nonlinear	DPS	In-domain	24.88	0.26	0.71	22.51	0.38	0.63	20.31	0.39	0.54
		CelebA	25.21	0.27	0.74	22.34	0.47	0.63	20.52	0.51	0.52
	Ours	Bedroom	24.59	0.39	0.69	22.67	0.39	0.64	20.79	0.47	0.54
		Church	24.73	0.39	0.69	22.59	0.42	0.63	20.88	0.39	0.56

Table 6: Comparison with DMPlug under in-domain priors for inpainting and super-resolution task.

Task	Dataset	Ours			DMPlug		
		PSNR ↑	LPIPS ↓	SSIM ↑	PSNR ↑	LPIPS ↓	SSIM ↑
Gaussian	CelebA	29.98	0.21	0.82	29.52	0.23	0.81
	Church	22.43	0.30	0.62	22.24	0.32	0.61
	Bedroom	25.28	0.30	0.72	25.08	0.33	0.71
Super-Res	CelebA	31.271	0.184	0.863	31.122	0.198	0.857
	Church	23.088	0.266	0.674	23.183	0.280	0.667
	Bedroom	26.587	0.249	0.777	26.309	0.280	0.767

C.2 Comparison with Optimization-Based Methods

Table 6 reports further comparisons between our method and DMPlug (Wang et al., 2024) on inpainting and 4× super-resolution. Across both tasks and all three datasets, our method matches or outperforms DMPlug. For inpainting, we achieve improvements on CelebA and Bedroom, respectively, along with consistently lower LPIPS and higher SSIM. On Church inpainting, the two methods perform nearly identically in PSNR, while our approach still yields better perceptual quality.

C.3 Failure Modes

Table 7 provides the full quantitative results for box inpainting, where the goal is to reconstruct Church images while masking increasingly large square regions. For moderate mask sizes (0.3×0.3 and 0.4×0.4), our in-domain weak prior remains competitive with DPS. However, as the masked region grows to 0.5×0.5 and 0.6×0.6 , DPS begins to dominate in both PSNR and LPIPS, while our in-domain variant exhibits noticeable

Table 7: Failure mode results for box inpainting.

Mask	Method	PSNR \uparrow	LPIPS \downarrow	SSIM \uparrow
0.3 \times 0.3	DPS	25.00	0.22	0.79
	Ours (In)	25.28	0.23	0.81
	Ours (Out)	22.42	0.32	0.77
0.4 \times 0.4	DPS	22.28	0.24	0.76
	Ours (In)	22.31	0.25	0.78
	Ours (Out)	19.20	0.35	0.73
0.5 \times 0.5	DPS	19.38	0.27	0.71
	Ours (In)	19.09	0.30	0.72
	Ours (Out)	16.81	0.39	0.67
0.6 \times 0.6	DPS	17.72	0.30	0.65
	Ours (In)	17.27	0.34	0.66
	Ours (Out)	15.35	0.43	0.61

degradation, as illustrated in the additional visualizations in Figure 14. This confirms the conclusion that weak diffusion priors remain effective for reconstruction-focused inverse problems but encounter fundamental limitations in generation-heavy settings.

We observe a similar trend for large-scale super-resolution. Qualitative results for 16 \times super-resolution are shown in Figure 15, where out-of-domain reconstructions generated by a CelebA-pretrained model begin to exhibit face-like structures when applied to Church images.

C.4 Latent Diffusion Applications

We evaluate two few-step priors based on Stable Diffusion 2.1 and DiT, and compare against two baselines: DPS [Chung et al. \(2023\)](#) and DSG [Yang et al. \(2024\)](#), all implemented with SD 2.1 backbones.

Table 8 summarizes ImageNet results for inpainting and Gaussian deblurring using latent diffusion models. Overall, our method performs comparably to DPS on both tasks and substantially outperforms DSG. Even with much weaker generative models, our framework preserves strong reconstruction quality for both inpainting and deblurring. Visual comparisons are provided in Figure 13 (Gaussian deblurring) and Figure 12 (inpainting).

C.5 On computational comparability with baseline algorithms

Our method and DMPlug both use the same initial-noise optimization framework, so we use the exact same optimization budget in all comparisons to ensure fairness.

Table 8: Results for inpainting and Gaussian deblurring. We report ES metrics when available; otherwise, final results are used. Best results are in **bold**, second-best are underlined.

Task	Method	Model	PSNR \uparrow	LPIPS \downarrow	SSIM \uparrow
Inpainting	Ours	DiT	28.44	0.394	0.727
		SD2.1	26.82	<u>0.374</u>	<u>0.745</u>
	DPS		<u>28.21</u>	0.292	0.797
		SD2.1	23.33	0.503	0.597
	DSG	DiT	26.48	0.458	0.678
		SD2.1	25.40	<u>0.443</u>	<u>0.685</u>
Gaussian	Ours	DiT	25.49	0.388	0.728
		SD2.1	22.09	0.510	0.539
	DPS				
		SD2.1			

DPS and our method allocate computation in fundamentally different ways, so a strict compute-matched comparison is not straightforward. More precisely

- DPS has an essentially fixed per-run cost once the number of reverse diffusion steps is set: each reverse step involves roughly one denoiser evaluation, so the total cost is driven by the chain length. Moreover, existing studies [Ma et al. \(2025\)](#) suggest that increasing the chain length scales poorly, so the DPS budget is typically treated as effectively fixed. People typically choose 500 or 1000 reverse steps depending on the task.
- Our method has a tunable compute budget through the number of initial-noise optimization iterations. Each iteration requires running a K -step DDIM generation, so the dominant cost scales with the product of the iteration count and the DDIM step count. In our experiments, we typically use a 3-step DDIM and 500 iterations of optimization.

In our experiments in Section 4, a single run of the initial-noise optimization method costs about $1.5\times$ to $3\times$ as much compute as a single DPS run. We believe this is still appropriate for the goal of the comparison. First, we use empirical performance to show that weak priors can solve inverse problems in data-informative regimes, rather than to claim that our method is uniformly superior to DPS. The focus is on qualitative behavior and reconstruction metrics (e.g., PSNR/SSIM), not on a compute-matched efficiency benchmark. Second, once the diffusion chain length is fixed, DPS does not offer a directly comparable knob for “scaling up” with additional compute. For completeness, we therefore also include an explicitly compute-matched comparison, described below.

Figure 5 compares DPS and initial-noise optimization under a matched compute budget, measured by the number of denoiser evaluations. We evaluate PSNR and SSIM

Table 9: Measurement operators and degradation models used in the experiments.

Task	Operator	Parameters
Inpainting	Random masking	70% of pixels removed
Gaussian Deblurring	Gaussian convolution	Kernel size = 61, intensity = 3
Super Resolution	Downsampling	Factor 4 \times
Nonlinear Deblurring	BKSE (GOPRO_wVAE.pth)	Pretrained GoPro wave model

on the FFHQ (human faces) dataset [Karras et al. \(2019\)](#) by averaging metrics over test images. For DPS, we consider two configurations with 100 and 1000 diffusion steps. Under a fixed budget (e.g., 10,000 denoiser evaluations), we implement a best-of- N strategy for DPS: for each test image, we run each DPS configuration N times (e.g., 10 runs for the 1000-step chain or 100 runs for the 100-step chain), keep the best reconstruction among the N outputs, and then average the resulting metrics across the dataset. The results again show a clear advantage for initial-noise optimization in this compute-matched setting.

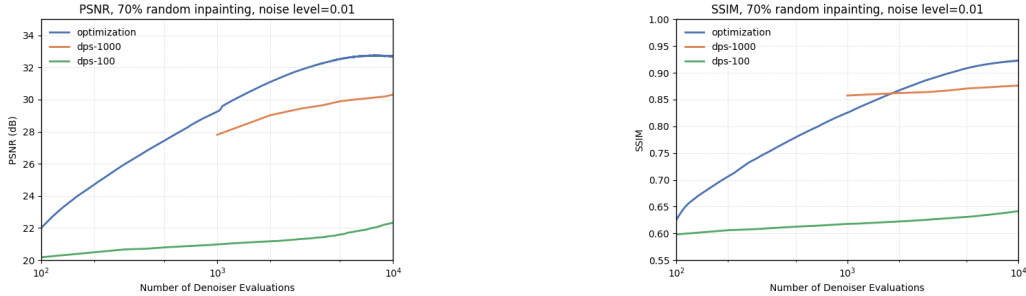


Figure 5: Compute-matched comparison between DPS and initial-noise optimization methods.

C.6 Experiment Configuration

Forward Operator The forward operators tested are inpainting, Gaussian deblurring, super-resolution, and nonlinear deblurring, and the detailed setup is summarized in Table 9. All measurements have additive Gaussian noise with $\sigma = 0.01$. The nonlinear blur model follows [Tran et al. \(2021\)](#) available on public GitHub repository <https://github.com/VinAIResearch/blur-kernel-space-exploring>.

Non-latent Diffusion For non-latent diffusion settings, DPS was executed with 1000 sampling steps, while both DMPlug and our proposed method employed 1000 optimization steps. All experiments used Hugging Face pretrained diffusion models on the Church, Bedroom, and CelebA-HQ datasets available with ID `google/ddpm-church-256`, `google/ddpm-bedroom-256`, and `google/ddpm-celebahq-256`. We adopted task-specific learning rates and HOLDOUTTOPK ratios as reported in Table 10. DPS and DMPlug are

Table 10: Algorithm hyperparameters for each measurement task.

Task	Learning Rate	k for HoldoutTopK
Inpainting	0.02	90% / 10%
Gaussian Deblurring	0.02	80% / 20%
Super Resolution	0.01	95% / 5%
Nonlinear Deblurring	0.01	90% / 10%

implemented under their default configs.

Latent Diffusion For latent diffusion experiments, all baseline methods (DPS and DSG) used 500 steps. Our approach used 500 optimization steps. The learning rate for our approach was set to 0.1 for DiT and 0.2 for Stable Diffusion 2.1. All models were used with a null prompt as an empty text prompt or class 1000.

Baselines’ implementation is available on the public GitHub repository <https://github.com/tongdaxu/diffusers-Diffusion-Posterior-Sampling> , which provides diffuser-based implementations of three algorithms with default configurations.

Stable Diffusion 2.1 is available on Hugging Face with ID *Manojb/stable-diffusion-2-1-base*. The DiT model is in the official release at <https://github.com/facebookresearch/DiT>, and we use the (512×512) resolution model.

All experiments were conducted on eight NVIDIA L40S GPUs. The most computationally intensive configuration, Stable Diffusion with optimization-based reconstruction, required approximately seven minutes to reconstruct a single image using 500 steps.

D Visualization

D.1 Reconstruction Process with Different Priors

Figures 6–11 show results of our initial-noise optimization algorithm for recovering images using both in-distribution and out-of-distribution priors.

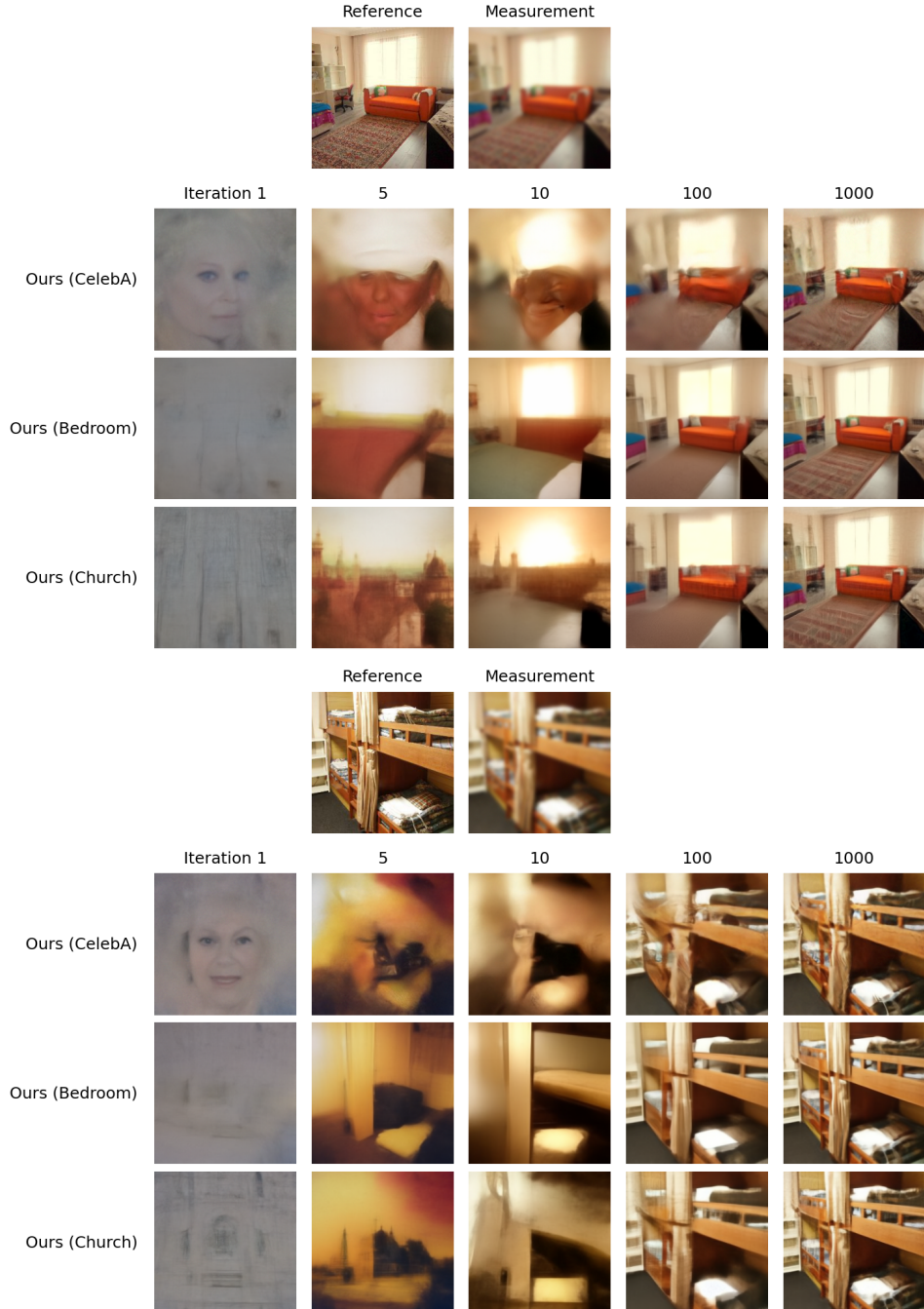


Figure 6: Bedroom reconstruction results for Gaussian deblurring.



Figure 7: Bedroom reconstruction results for inpainting.

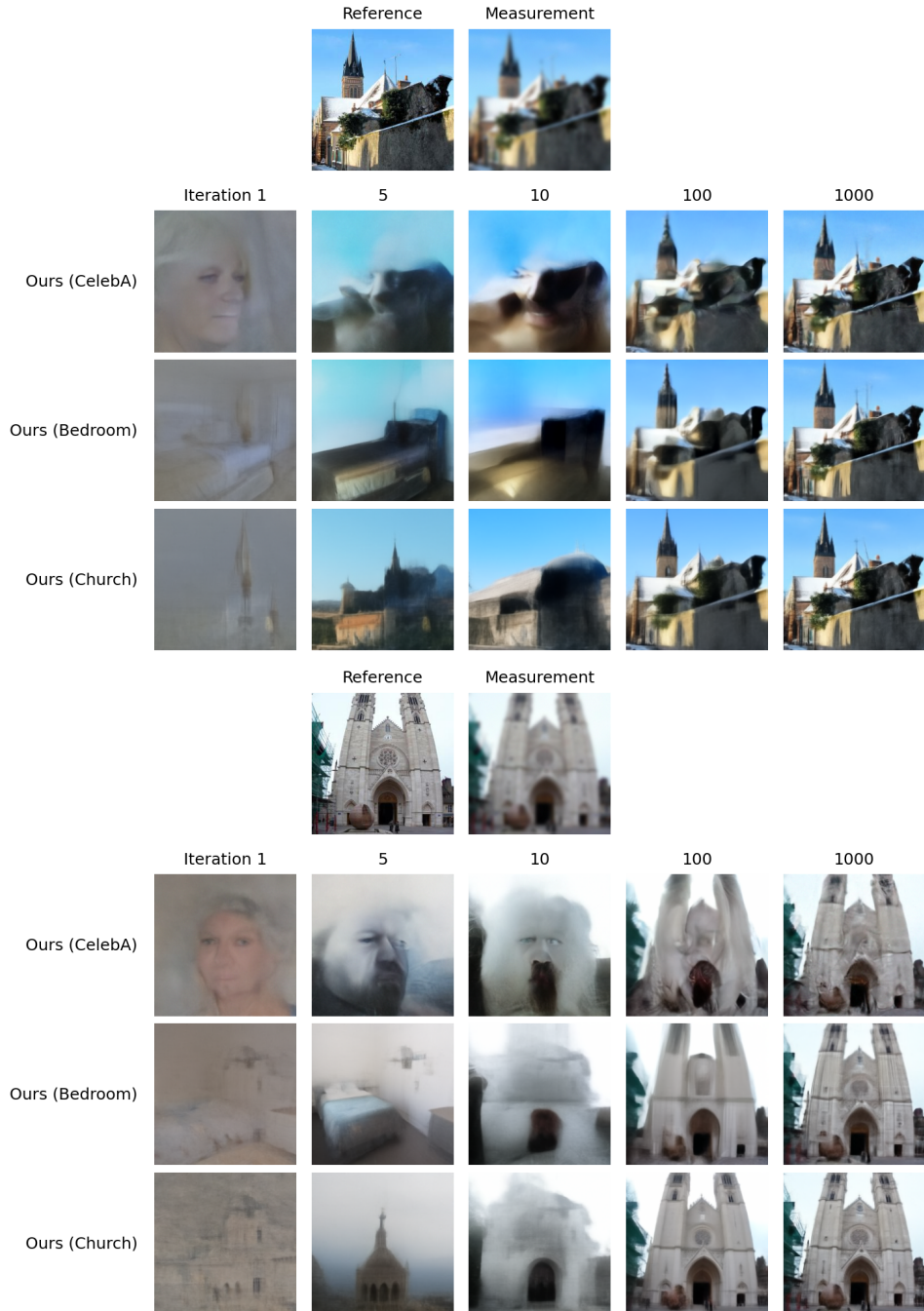


Figure 8: Church reconstruction results for Gaussian deblurring.

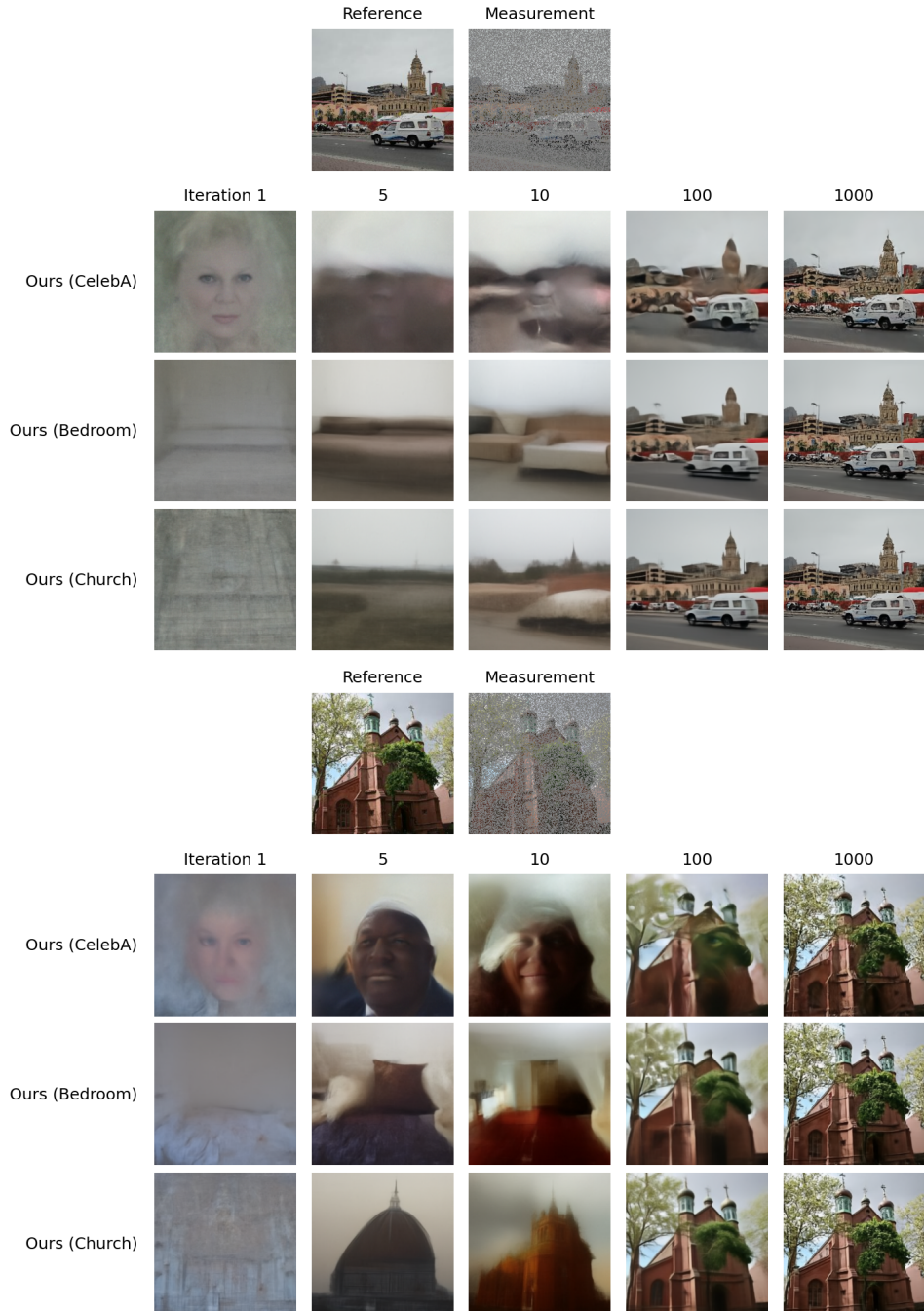


Figure 9: Church reconstruction results for inpainting.

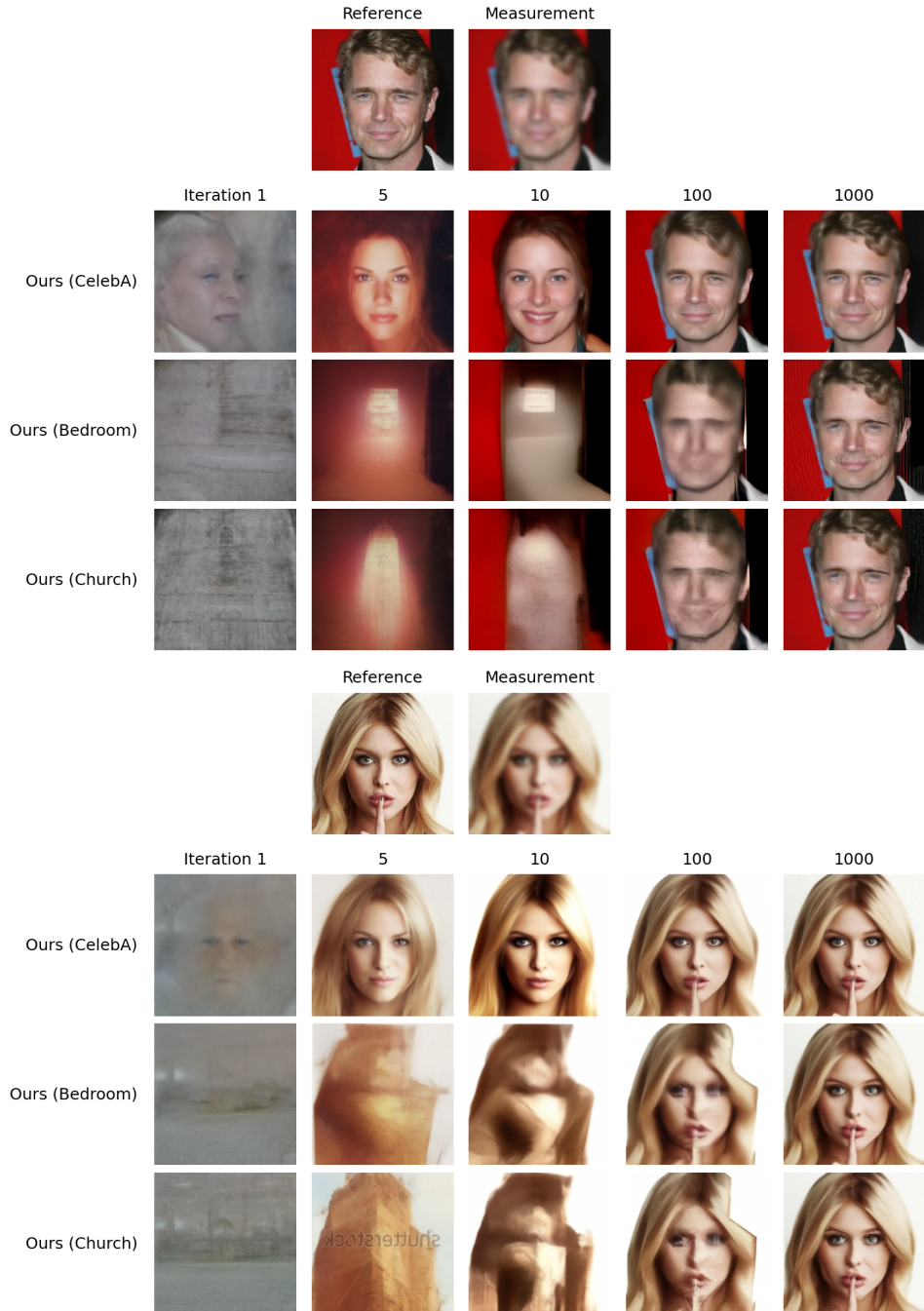


Figure 10: CelebA reconstruction results for Gaussian deblurring.

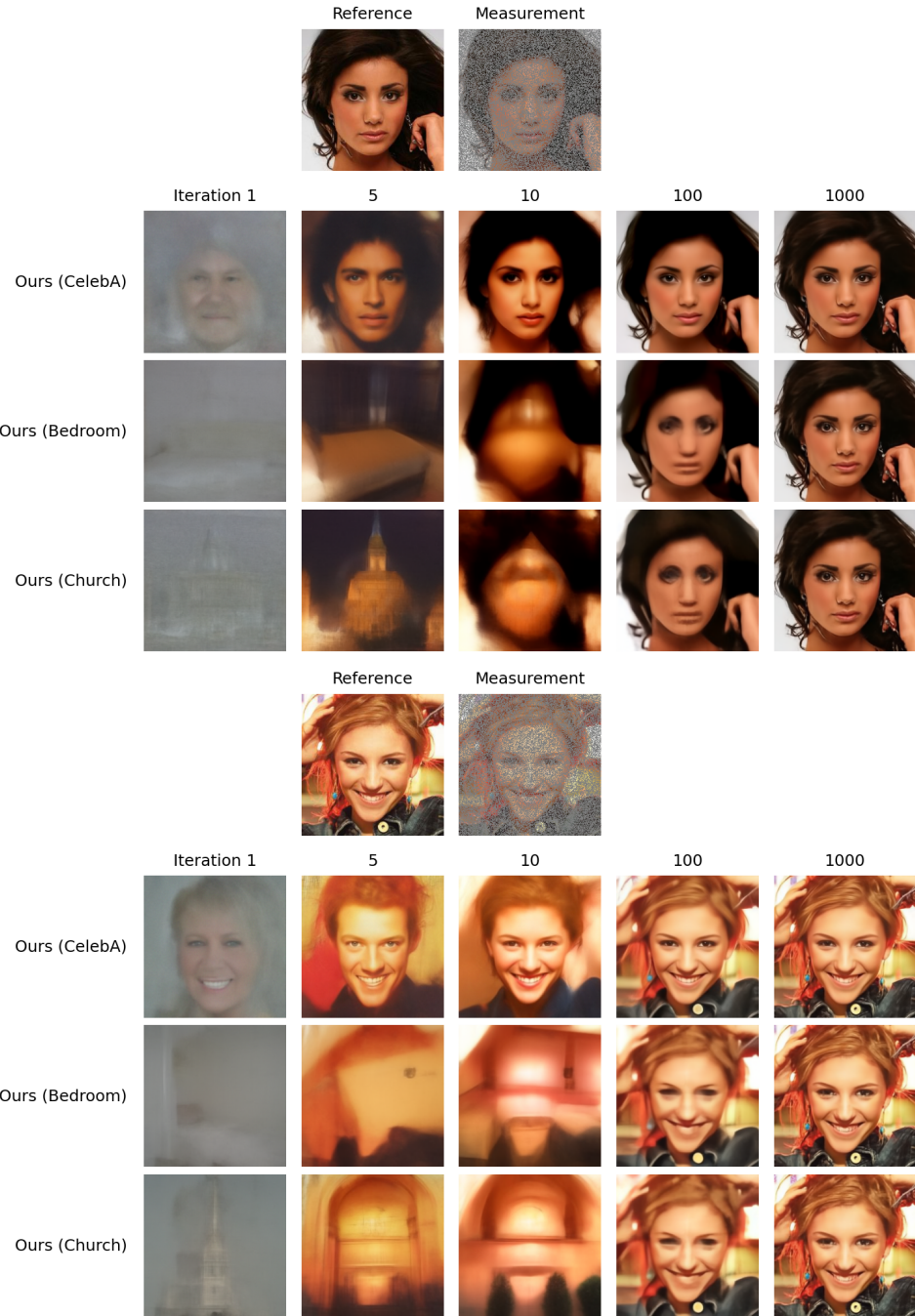


Figure 11: CelebA reconstruction results for inpainting.

D.2 Reconstruction Result for Latent Diffusion Application

Figures 12 and 13 show reconstruction results for several latent diffusion algorithms. We implement our methods using both SD2.1 and DiT priors.

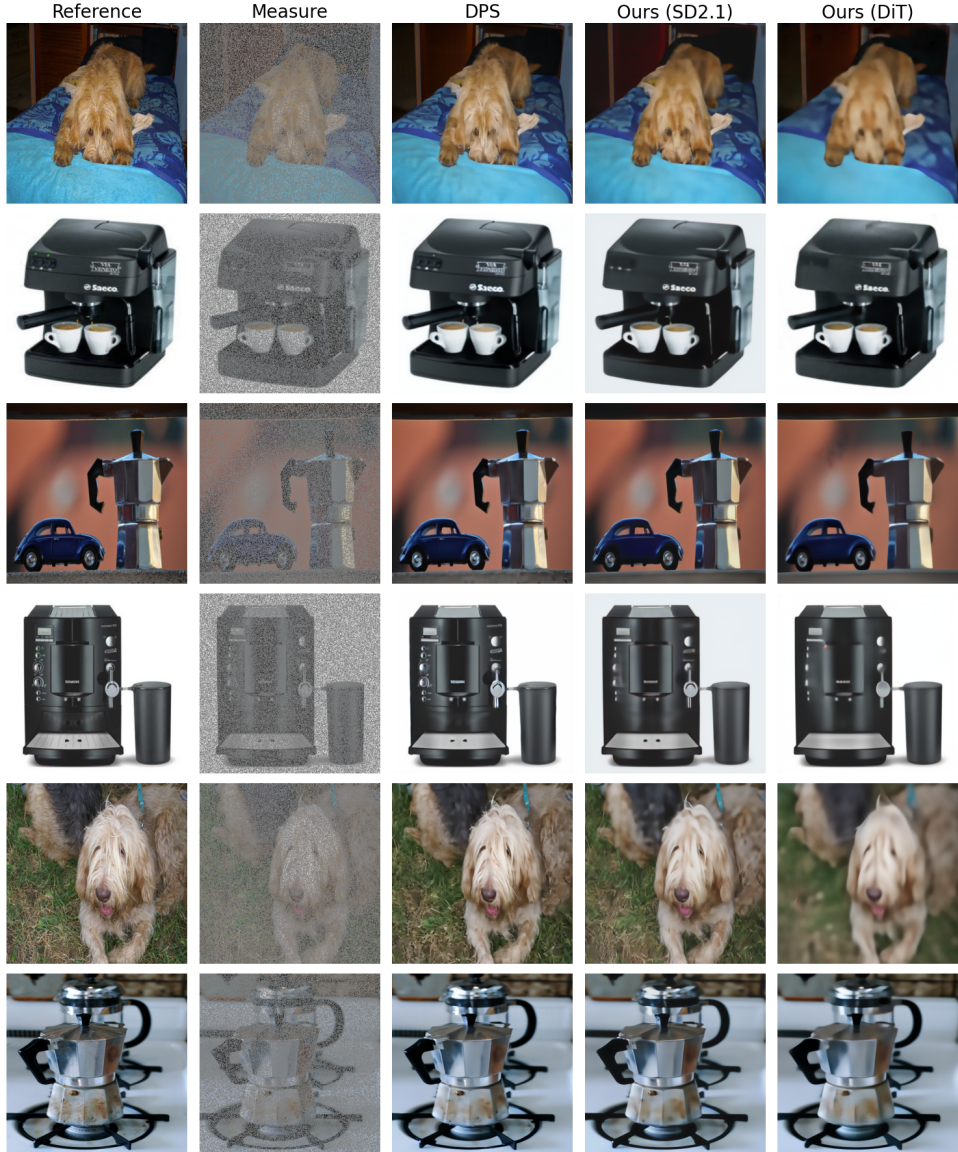


Figure 12: Reconstruction results for inpainting task on ImageNet using latent diffusion priors (Stable Diffusion 2.1 and DiT), compared with DPS

D.3 Reconstruction Failure Case

Figures 14 and 15 visualize box inpainting and super-resolution results for DPS and our method. Our method is shown with both in-domain and out-of-domain weak priors. The failure mode is evident from the reconstruction inconsistencies.

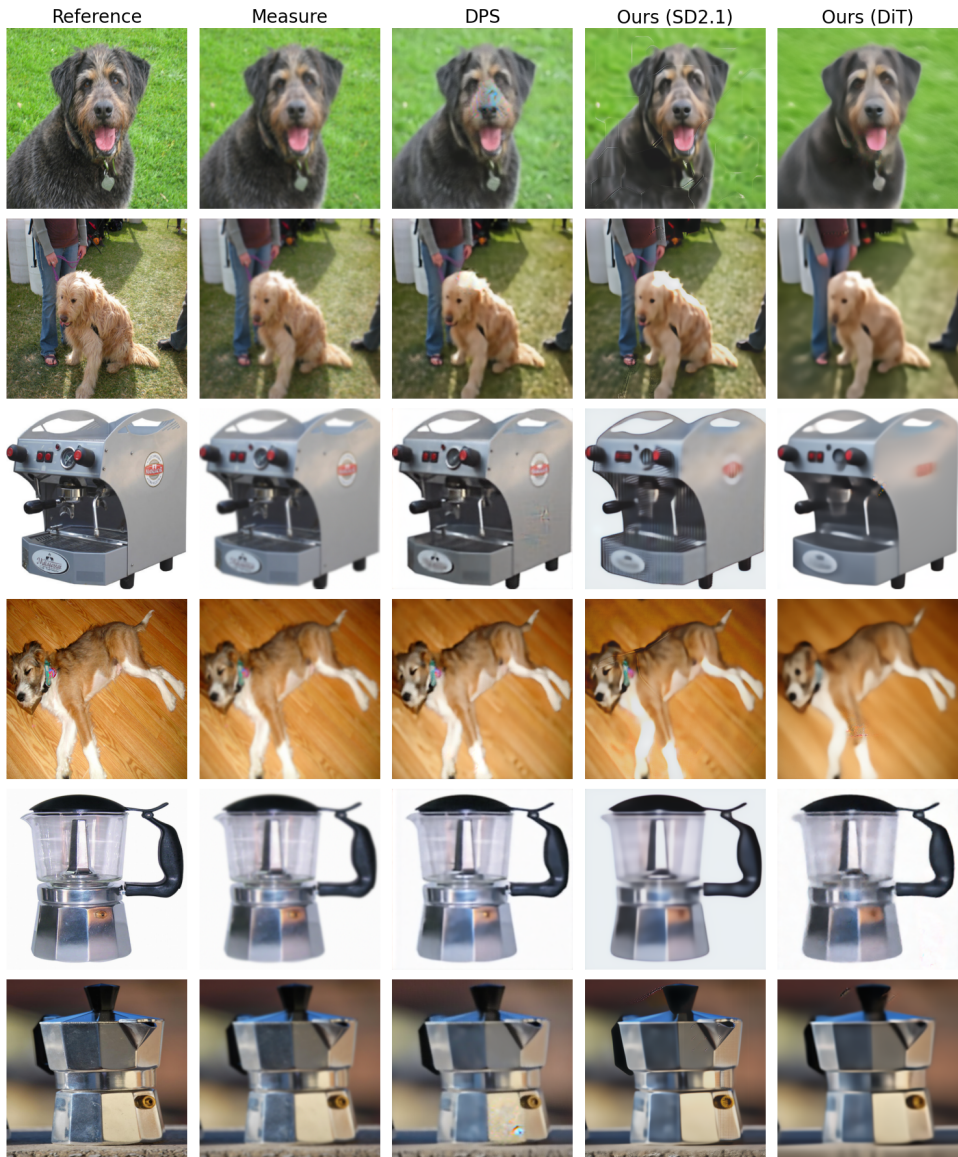


Figure 13: Reconstruction results for Gaussian deblurring task on ImageNet using latent diffusion priors (Stable Diffusion 2.1 and DiT), compared with DPS

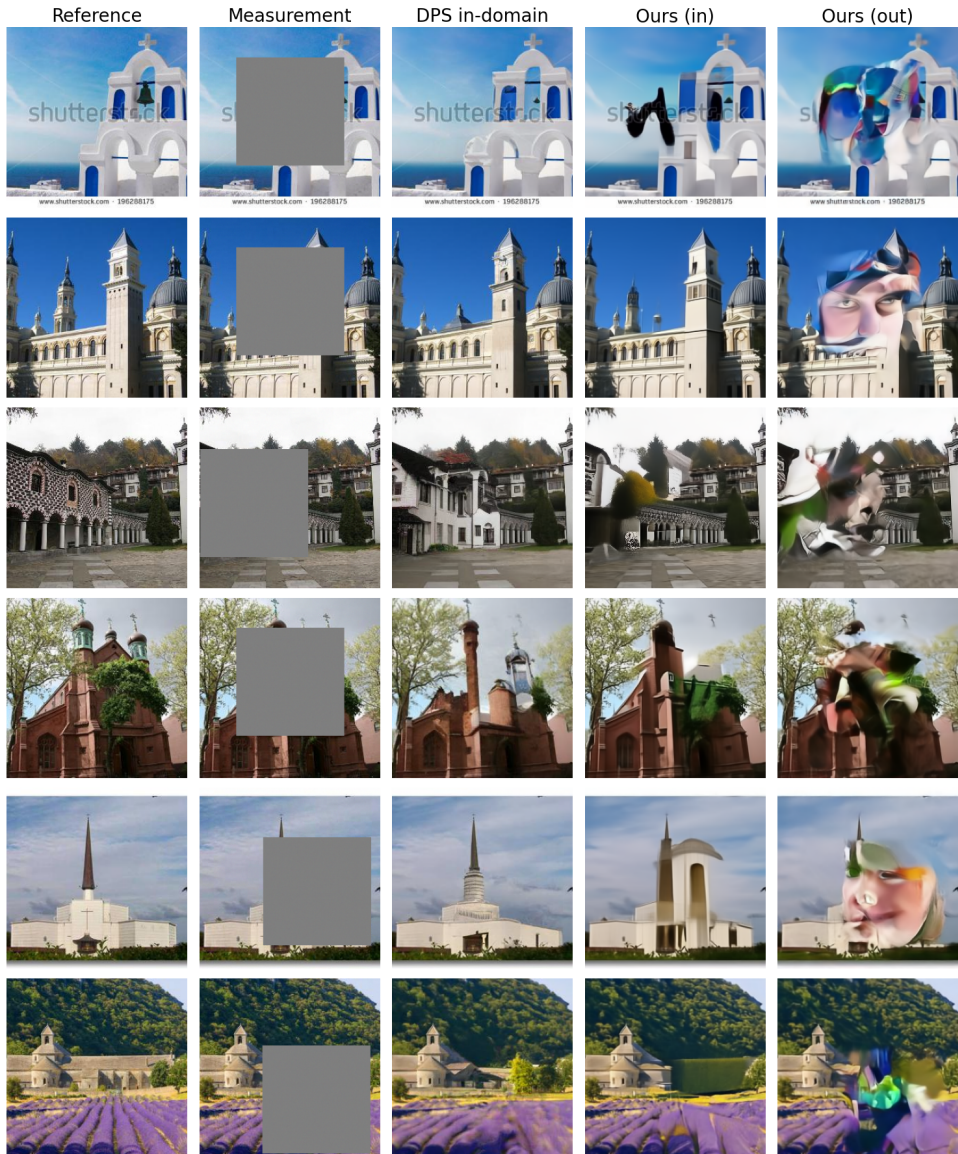


Figure 14: Sample qualitative reconstruction results for box inpainting with a 0.6×0.6 mask. DPS and Ours (in) uses Church pretrained model, Ours (out) uses CelebA pretrained model.

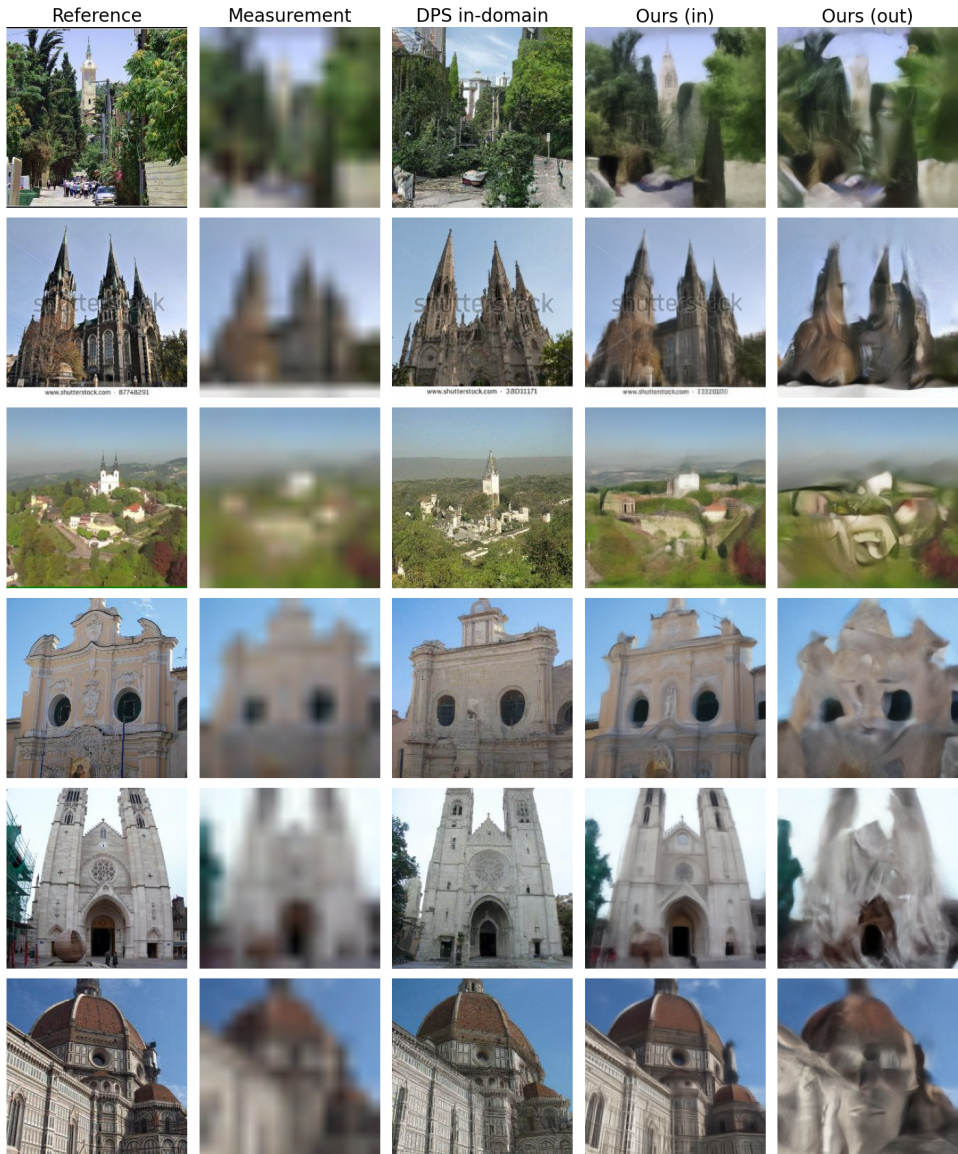


Figure 15: Sample qualitative reconstruction results for super-resolution with x16 ratio. DPS and Ours (in) uses Church pretrained model, Ours (out) uses CelebA pretrained model.